



BALLOON-BORNE SUBMILLIMETER POLARIMETRY OF THE VELA C MOLECULAR CLOUD: SYSTEMATIC DEPENDENCE OF POLARIZATION FRACTION ON COLUMN DENSITY AND LOCAL POLARIZATION-ANGLE DISPERSION

LAURA M. FISSEL¹, PETER A. R. ADE², FRANCESCO E. ANGILÈ³, PETER ASHTON¹, STEVEN J. BENTON^{4,5}, MARK J. DEVLIN³,
BRADLEY DOBER³, YASUO FUKUI⁶, NICHOLAS GALITZKI³, NATALIE N. GANDILO^{7,8}, JEFFREY KLEIN³, ANDREI L. KOROTKOV⁹,
ZHI-YUN LI¹⁰, PETER G. MARTIN¹¹, TRISTAN G. MATTHEWS¹, LORENZO MONCELSI¹², FUMITAKA NAKAMURA¹³,
CALVIN B. NETTERFIELD^{4,7}, GILES NOVAK¹, ENZO PASCALE², FRÉDÉRIK POIDEVIN^{14,15}, FABIO P. SANTOS¹, GIORGIO SAVINI¹⁶,
DOUGLAS SCOTT¹⁷, JAMIL A. SHARIF^{7,18}, JUAN DIEGO SOLER¹⁹, NICHOLAS E. THOMAS²⁰, CAROLE E. TUCKER²,
GREGORY S. TUCKER⁹, AND DEREK WARD-THOMPSON²¹

¹ Center for Interdisciplinary Exploration and Research in Astrophysics (CIERA) and Department of Physics and Astronomy, Northwestern University, 2145 Sheridan Road, Evanston, IL 60208, USA

² Cardiff University, School of Physics and Astronomy, Queens Buildings, The Parade, Cardiff, CF24 3AA, UK

³ Department of Physics and Astronomy, University of Pennsylvania, 209 South 33rd Street, Philadelphia, PA, 19104, USA

⁴ Department of Physics, University of Toronto, 60 St. George Street, Toronto, ON M5S 1A7, Canada

⁵ Department of Physics, Princeton University, Jadwin Hall, Princeton, NJ 08544, USA

⁶ Department of Physics and Astrophysics, Nagoya University, Nagoya 464-8602, Japan

⁷ Department of Astronomy and Astrophysics, University of Toronto, 50 St. George Street, Toronto, ON M5S 3H4, Canada

⁸ Department of Physics and Astronomy, Johns Hopkins University, 3701 San Martin Drive, Baltimore, Maryland, USA

⁹ Department of Physics, Brown University, 182 Hope Street, Providence, RI, 02912, USA

¹⁰ Department of Astronomy, University of Virginia, 530 McCormick Rd, Charlottesville, VA 22904, USA

¹¹ CITA, University of Toronto, 60 St. George St., Toronto, ON M5S 3H8, Canada

¹² California Institute of Technology, 1200 E. California Blvd., Pasadena, CA, 91125, USA

¹³ National Astronomical Observatory, Mitaka, Tokyo 181-8588, Japan

¹⁴ Instituto de Astrofísica de Canarias, E-38200 La Laguna, Tenerife, Spain

¹⁵ Universidad de La Laguna, Dept. Astrofísica, E-38206 La Laguna, Tenerife, Spain

¹⁶ Department of Physics and Astronomy, University College London, Gower Street, London, WC1E 6BT, UK

¹⁷ Department of Physics and Astronomy, University of British Columbia, 6224 Agricultural Road, Vancouver, BC V6T 1Z1, Canada

¹⁸ Department of Physics, Case Western Reserve University, 2076 Adelbert Road, Cleveland Ohio, 44106-7079, USA

¹⁹ Institut d'Astrophysique Spatiale, CNRS (UMR8617) Université Paris-Sud 11, Bâtiment 121, Orsay, France

²⁰ NASA/Goddard Space Flight Center, Greenbelt, MD 20771, USA

²¹ Jeremiah Horrocks Institute, University of Central Lancashire, PR1 2HE, UK

Received 2015 September 6; revised 2016 February 21; accepted 2016 April 26; published 2016 June 21

ABSTRACT

We present results for Vela C obtained during the 2012 flight of the Balloon-borne Large Aperture Submillimeter Telescope for Polarimetry. We mapped polarized intensity across almost the entire extent of this giant molecular cloud, in bands centered at 250, 350, and 500 μm . In this initial paper, we show our 500 μm data smoothed to a resolution of $2/5$ (approximately 0.5 pc). We show that the mean level of the fractional polarization p and most of its spatial variations can be accounted for using an empirical three-parameter power-law fit, $p \propto N^{-0.45} S^{-0.60}$, where N is the hydrogen column density and S is the polarization-angle dispersion on 0.5 pc scales. The decrease of p with increasing S is expected because changes in the magnetic field direction within the cloud volume sampled by each measurement will lead to cancellation of polarization signals. The decrease of p with increasing N might be caused by the same effect, if magnetic field disorder increases for high column density sightlines. Alternatively, the intrinsic polarization efficiency of the dust grain population might be lower for material along higher density sightlines. We find no significant correlation between N and S . Comparison of observed submillimeter polarization maps with synthetic polarization maps derived from numerical simulations provides a promising method for testing star formation theories. Realistic simulations should allow for the possibility of variable intrinsic polarization efficiency. The measured levels of correlation among p , N , and S provide points of comparison between observations and simulations.

Key words: dust, extinction – instrumentation: polarimeters – ISM: individual objects (Vela C) – ISM: magnetic fields – stars: formation – techniques: polarimetric

1. INTRODUCTION

The Balloon-borne Large Aperture Submillimeter Telescope for Polarimetry (BLASTPol; Galitzki et al. 2014) is sensitive to magnetic field structure ranging from scales of entire giant molecular clouds (GMCs) down to cores (for nearby clouds). In this paper we present a very sensitive survey of the star-forming region Vela C from the 2012 flight of BLASTPol. Our goal is to quantify the dependence of polarization fraction on column density, temperature, and local magnetic field disorder,

in order to provide empirical formulae that can be used to test numerical simulations of molecular clouds. These observations are timely because the role that magnetic fields play in the formation of molecular clouds and their substructures persists as an outstanding question in the understanding of the detailed mechanics of star formation (McKee & Ostriker 2007). Strong magnetic fields that are well coupled to the gas can inhibit or slow down gravitational collapse of gas in the direction perpendicular to the cloud magnetic field lines (Mouschovias &

Ciolek 1999). This in turn can contribute to the low observed star formation efficiency seen in molecular clouds. Numerical simulations of molecular clouds show that magnetized clouds differ from unmagnetized clouds in cloud density contrasts (Kowal et al. 2007) and in star formation efficiency (Myers et al. 2014). However, obtaining detailed measurements of magnetic fields in molecular clouds over a wide range of relevant spatial and density scales remains challenging.

Zeeman splitting in molecular lines can be used to measure the component of magnetic field strength parallel to the line of sight directly (Crutcher 2012). However this technique is challenging as the Doppler broadening of molecular lines is generally much larger than the Zeeman splitting. After many years of careful observations there are now several dozen detections of Zeeman splitting in molecular lines that trace dense gas (Crutcher 2012).

An alternative method for studying magnetic fields in molecular clouds is to use polarization maps to infer the orientation of the magnetic field projected on the plane of the sky (Φ). Dust grains are believed to align with their long axes on average perpendicular to the local magnetic field (see Lazarian 2007 for a review). Current evidence suggests that radiative torques (RATs) from anisotropic radiation fields might be the dominant alignment mechanism (Lazarian & Hoang 2007; Andersson et al. 2015). Optical and near-IR light from stars that passes through a foreground cloud of aligned dust grains becomes polarized parallel to Φ . This method has long been used to study the magnetic field orientation in the diffuse ISM (Hall 1949; Hiltner 1949; Heiles 2000), but is not easily applicable for high extinction cloud sightlines. However, dust grains emit radiation preferentially polarized parallel to their long axes, so that the resulting far-infrared/submillimeter thermal emission is polarized orthogonal to Φ (Hildebrand 1988). The emission is generally optically thin.

The fraction of dust emission that is polarized (p), does not give any direct estimate of the magnetic field strength. However, it can encode information about the dust grain shape and alignment efficiency, angle of the field with respect to the line of sight, and changes in field direction. Hildebrand (1988) reviews the factors that affect p for optically thin thermal emission from a population of grains. First, consider the case of perfect spinning alignment of an ensemble of identical grains in a uniform magnetic field oriented orthogonally to the line of sight ($\gamma = 0^\circ$). In this case p will be determined by the grains' optical constants and shape (e.g., ratio of axes for the case of oblate spheroids). Next, if the grain spin axes are not all exactly parallel to the ambient field, the polarization will be reduced by what is known as the Rayleigh reduction factor (Greenberg 1968, pp. 221–230; Lazarian 2007). For this paper we define the “intrinsic polarization efficiency” as the polarization p of the emission from such an ensemble of imperfectly aligned grains. The measured polarization fraction can be less than this intrinsic polarization efficiency if there are variations in magnetic field direction within the conical volume being sampled by an observation. Finally, for arbitrary values of γ , the polarization is proportional to $\cos^2(\gamma)$.

Comparisons between statistical properties of observed polarization maps and synthetic observations of 3D numerical models of star formation are a promising method for constraining molecular cloud physics. Examples include Falceta-Gonçalves et al. (2008) as well as histograms of relative orientations (HRO, Soler et al. 2013; Planck Collaboration Int. XXXV 2016). If the intrinsic polarization

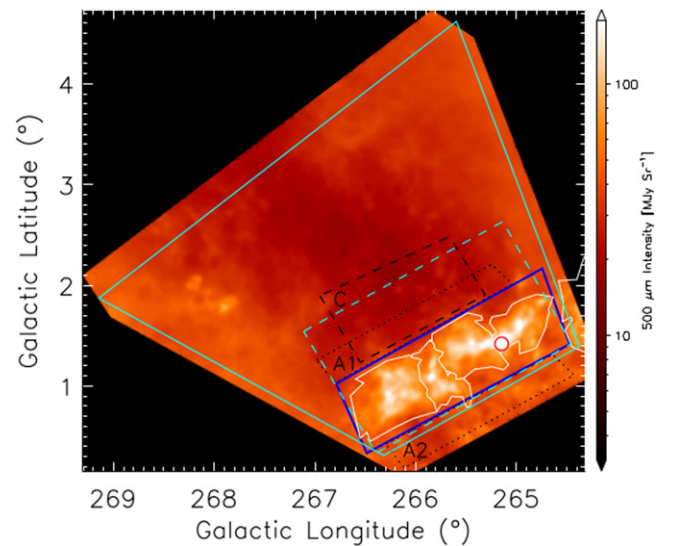


Figure 1. BLASTPol 500 μm I map of Vela C and surroundings. Cyan lines show the boundaries of the two raster scan regions used to make the maps in this paper: the region marked with cyan dashes was observed for 43 hr, while the solid cyan lines show a larger region covering Vela C and surrounding diffuse emission, which was observed for 11 hr in total. Also shown are the locations of the regions used in the diffuse emission subtraction for the BLASTPol I , Q , and U maps as described in Section 3.5. The region labeled C is used in the “conservative” diffuse emission subtraction method. The “aggressive” method used the two regions labelled A1 and A2. Cloud subregions defined by Hill et al. (2011) are indicated in white contours. The region outlined in blue shows the “validity region” where the null tests discussed in Section 3.6 were passed, and where both diffuse emission subtraction methods discussed in Section 3.5 are valid; only polarization measurements within this validity region are used for science analysis in later sections. The red circle shows the area near RCW 36 excluded from our polarization analysis because of large Stokes I , Q , and U null test residuals.

efficiency varies within the cloud, then measurements of the inferred magnetic field orientation will be weighted toward the field orientation in regions along the line of sight where the intrinsic polarization efficiency is high. To use polarization observations to constrain the structure of the magnetic field in star-forming clouds it is therefore important to understand how the intrinsic polarization efficiency varies within molecular clouds.

The Vela C GMC was discovered by Murphy & May (1991) via CO observations of a larger scale structure known as the Vela Molecular Ridge. Vela C was later observed in the submillimeter by Netterfield et al. (2009) and was found to be a cool molecular cloud in an early evolutionary state. At a distance of 700 ± 200 pc (Liseau et al. 1992), the cloud subtends 3° on the sky (35 pc), and contains a large quantity of dense gas ($M \approx 5 \times 10^4 M_\odot$ as traced by C^{18}O 1-0 observations from Yamaguchi et al. 1999). A *Herschel*²² survey of Vela C by Hill et al. (2011) showed that the cloud could be divided into five subregions at an $A_V = 7$ mag threshold as shown in Figure 1. These subregions show a range of cloud substructures, from the apparently cold network of overlapping filaments in the South-Nest subregion, to the high mass Center-Ridge, which contains a compact H II region, RCW 36.

This paper presents an overview of the BLASTPol 500 μm maps of Vela C from the 2012 flight.

²² *Herschel* is an ESA space observatory with science instruments provided by European-led Principal Investigator consortia and with important participation from NASA.

BLASTPol polarization data at $250\ \mu\text{m}$ and $350\ \mu\text{m}$ are discussed in a separate paper on the polarization spectrum of Vela C (Gandilo et al. submitted). In Section 2 we describe the BLASTPol telescope and BLASTPol 2012 science flight. Section 3 gives an overview of the data analysis pipeline and Section 4 presents the BLASTPol $500\ \mu\text{m}$ polarization maps. For comparison with the BLASTPol polarization data we used spectral energy distribution fits to the well-calibrated, higher resolution *Herschel* SPIRE and PACS maps to produce maps of Vela C column density (N) and dust temperature (T) as described in Section 5. We then examine the correlations between the polarization fraction p and N and T in Section 6, and develop a two-variable power-law model of p as a function of N and the local polarization-angle dispersion S in Section 7. Finally, in Section 8, we discuss the implications of our power-law model and we place a rough upper limit on the degree to which reduced intrinsic polarization efficiency at high N might bias our polarization measurements toward lower density cloud regions. Our findings are summarized in Section 9.

2. OBSERVATIONS

BLASTPol is a high altitude balloon-borne polarimeter that utilizes a 1.8 m diameter aluminium parabolic primary mirror, and a 40 cm aluminium secondary mirror. Incoming light is directed onto a series of reimaging optics cooled to 1 K in a liquid nitrogen-helium cryostat (Galitzki et al. 2014). A series of dichroic filters direct light onto focal-plane arrays of bolometers (cooled below 300 mK), which are similar to those used by *Herschel* SPIRE (Griffin et al. 2002, 2003).

The use of dichroic filters allows BLASTPol to observe simultaneously in three frequency bands centered at 250, 350, and $500\ \mu\text{m}$. Unlike ground based telescopes it is not restricted to observe through narrow windows in the atmospheric transmission spectrum. Instead, BLASTPol observes in three wide frequency bands ($\Delta f/f \simeq 30\%$), which bracket the peak of 10–20 K thermal dust emission. A metal mesh polarizing grid is mounted in front of each detector array. The polarizing grid is patterned so that each adjacent detector samples only the vertical or horizontal component of the incoming radiation. In this way a single Stokes parameter (Q or U) can be measured in the time it takes light from a source to move from one bolometer to an adjacent bolometer (<1 second for typical scan speeds). A sapphire achromatic half-wave plate (hereafter HWP) provides additional polarization modulation (Moncelsi et al. 2014). A detailed description of the instrument and summary of the observations will appear in a forthcoming publication (F. Angilè et al. 2016, in preparation).²³ The present paper refers only to observations of Vela C and surrounding regions made during the 2012 flight.

BLASTPol was launched on 26 December 2012. The payload rose to an average altitude of 38.5 km above sea level and began science operations, taking data until cryogenics were depleted 12 days and 12 hr after launch. Our selection of target molecular clouds was informed by target distance, visibility from Antarctica, and cloud brightness. The nearby GMC Vela C was our highest priority target. The observations discussed in this paper include two types of scans as shown in Figure 1 (cyan lines). Most of the integration time (43 hr) was used to map a “deep” ($3.1\ \text{deg}^2$) quadrilateral region covering four of the five

cloud subregions defined by Hill et al. (2011).²⁴ A further 11 hr were spent mapping a larger ($\sim 10\ \text{deg}^2$) area that includes significant regions of low dust column where $A_V \sim 1$ according to extinction maps from Dobashi et al. (2005). The larger region was observed to reconstruct the map zero-intensity levels.

Observations were made in sets of four raster scans, where the HWP was rotated to one of four angles (0° , 22.5° , 45° , 67.5°) after every completed raster scan. A complete set of four scans typically required one hour. Scans were made while the source was rising and setting to maximize the range of parallactic angle.

As discussed in Section 3.2, the telescope beam was much larger than predicted by our optics model, with significant non-Gaussian structure. We smoothed our data to achieve an approximately round beam having a FWHM of 2.5 at $500\ \mu\text{m}$.

3. DATA ANALYSIS

In this section we give a brief overview of the BLASTPol data analysis pipeline and highlight differences from the 2010 data pipeline described in Matthews et al. (2014). An in-depth description of the data reduction pipeline and iterative mapmaker TOAST will be given in a forthcoming paper (S. Benton et al. 2016, in preparation).

3.1. Time Domain Preprocessing

Standard techniques were applied to the bolometer time-ordered data (hereafter TOD) to remove detector spikes (mostly due to cosmic rays), deconvolve the bolometer time constant, and remove an elevation-dependent feature (see Matthews et al. 2014). The data were further preprocessed by fitting and removing an exponential function fit to each detector’s TOD in the first 30 seconds after a HWP rotation or a telescope slew. A high-pass filter with power-law cutoff was used to whiten noise in the TOD below 5 mHz. Temporal gain variations were removed using the DC voltage level of each detector and periodic measurements of an internal calibration source. Pixel-to-pixel detector gain variations were corrected by frequent observations of the bright compact source IRAS 08470–4243.

Telescope attitude was reconstructed using pointing solutions generated from the BLASTPol optical star camera,²⁵ with payload rotational velocities from gyroscopes used to interpolate between pointing solutions (Pascale et al. 2008). Data having pointing uncertainties $>5''$ were discarded. The final on-sky pointing solution was calibrated to match the astrometry of publicly available *Herschel* SPIRE maps²⁶ at the same wavelength.

3.2. Beam Analysis

The BLASTPol 2012 beam differs from the beam predicted by our optics model. It has multiple elongated peaks, and the relative power in each peak varies from detector to detector. BLASTPol filters were designed for near-space conditions and the telescope far field is several kilometers away so it was not possible to map the far-field beam at sea level (Galitzki et al. 2014). Instead the beam had to be inferred from in-flight measurements of astronomical objects.

²⁴ The North region, as defined by Hill et al. (2011), has a significant spatial offset from the other four subregions and so was not included in our deep scan region.

²⁵ BLASTPol flew two redundant star-boresight optical star cameras during the 2012 flight, but one experienced a harddrive failure six hours after the launch (Galitzki et al. 2014).

²⁶ <http://www.cosmos.esa.int/web/herschel/science-archive>

²³ See also Matthews et al. (2014) for a description of the 2010 BLASTPol flight.

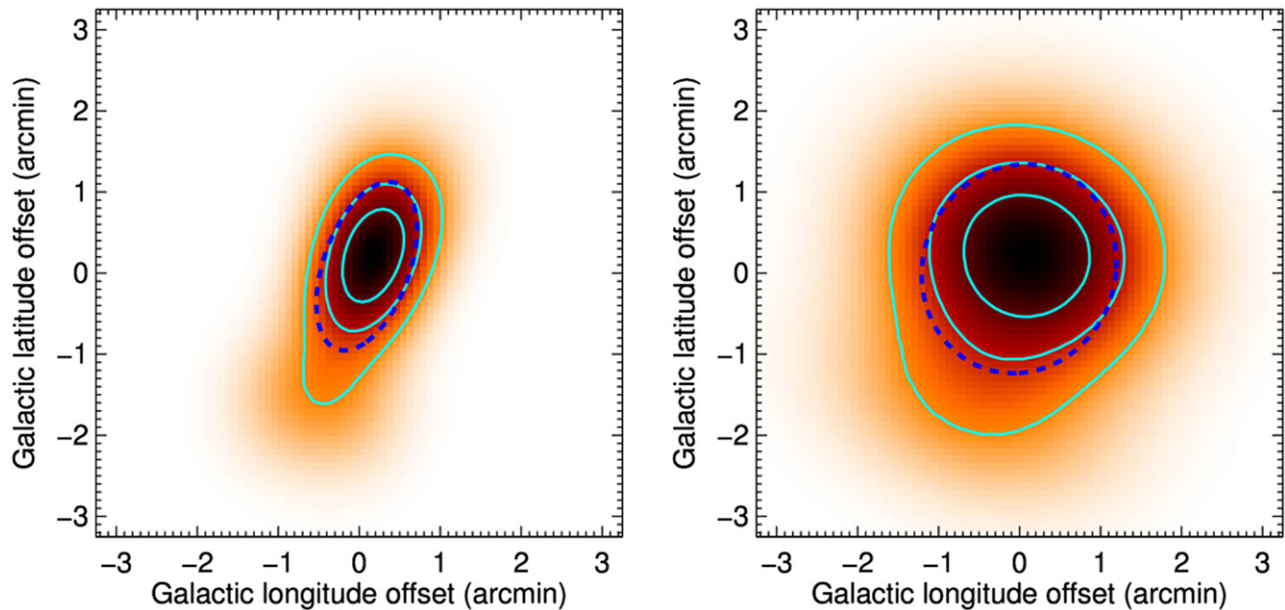


Figure 2. Left: BLASTPol $500\ \mu\text{m}$ beam model for the Vela C map. Right: BLASTPol $500\ \mu\text{m}$ beam model for the Vela C map after convolution with the smoothing kernel discussed in Section 3.2. Contour levels (cyan) are 25%, 50%, and 75% of the peak brightness. The dashed blue lines in each image show the FWHM of a fit to an elliptical Gaussian. FWHMs of the fitted Gaussians are $130''$ by $64''$ for the Vela C beam model (left panel) and $144''$ by $157''$ for the smoothed beam model (right panel).

Our 2012 instrument beam model was defined in telescope coordinates and was informed by observations of two objects: IRAS 08470–4243, a warm compact dust source located in the Vela Molecular Ridge; and limited observations of the planet Saturn made on 27 December 2015. IRAS 08470–4243 was observed every 4–8 hr, with reasonable coverage for all detectors, but it is not a point source at BLASTPol resolution. BLAST observations of IRAS 08470–4243 in 2006 found a FWHM of $\sim 40''$ (Netterfield et al. 2009). Saturn has a radius of 6×10^4 km, which corresponds to an angular size of $< 20''$, considerably smaller than the BLASTPol 2012 beam. Saturn was only observed early in the flight at telescope elevations of $< 25^\circ$ and was only fully mapped by the bolometers near the center of the focal plane arrays. Three elliptical Gaussians were fit to the Stokes I maps of IRAS 08470–4243 and Saturn. The free parameters were the Gaussian amplitudes, centroids, widths, and position angles. Only pixels above an intensity threshold of 20% of the peak intensity for IRAS 08470–4243 and 7.5% of the peak intensity for Saturn were used in the fits. The final 2012 instrument beam model used the centroid positions, amplitudes, and position angles from the fits to IRAS 08470–4243 and the Gaussian widths calculated from the fits to Saturn.

Next, an on-sky beam model was computed for the Vela C observations. The on-sky beam model is a time-weighted average of the instrument beam model rotated by the angle between the telescope vertical direction and Galactic north for each raster scan. The resulting average beam model for Vela C is shown in the left panel of Figure 2. A single elliptical Gaussian fit to this beam model gives FWHMs of $130''$ by $64''$, at position angle -51° . This beam is significantly larger than the expected diffraction limit of the telescope (FWHM = $60''$).

Lucy–Richardson (LR) deconvolution was previously used to correct a larger-than-expected beam from the BLAST 2005 flight (Roy et al. 2011). Here we used an iterative LR method and our beam model to deconvolve a simulated map consisting of a single Gaussian source with FWHM = $145''$. The deconvolved

map from this step when applied as a smoothing kernel to convolve the original beam model should restore the $145''$ Gaussian. The success of this step can be judged from the right panel in Figure 2: it does produce a single-peaked source that is approximately round (FWHM = $144''$ by $157''$). This same smoothing kernel was used to convolve the I , Q , and U maps of Vela C, with a resulting resolution of approximately 2.5 .

3.3. Instrumental Polarization

To determine the instrumental polarization (the polarization signal introduced by the instrument hereafter referred to as IP) we followed methods described in Matthews et al. (2014). In brief, the set of observations of Vela C was split into two bins based on parallactic angle, and maps were produced for each detector individually using the `naivepol` mapmaker (Moncelsi et al. 2014). The measured polarization is a superposition of one component fixed with respect to the sky and the IP, which is fixed with respect to the telescope. By comparing the polarization measurements at different parallactic angles the IP of each bolometer could be reconstructed. These IP terms were then removed during the mapmaking stage (Section 3.4). The $500\ \mu\text{m}$ array has an average IP amplitude of 0.53%. To check the effectiveness of the IP correction the Vela C data were divided into two halves and IP estimates derived from the first half of the data were used to correct the second half of the data. By measuring the IP of the “corrected” second half of the Vela C data we estimate that the minimum value of the fractional polarization p measurable by BLASTPol at $500\ \mu\text{m}$ is 0.1%.

3.4. TOAST

Maps were made using TOAST (Time Ordered Astrophysics Scalable Tools),²⁷ a collection of serial and OpenMP/MPI parallel tools for simulation and map making. Specifically, the

²⁷ <http://tskisner.github.io/TOAST>

generalized least-squares solver was used, which iteratively inverts the map-maker equation using the preconditioned conjugate gradient method (see Cantalupo et al. 2010, a predecessor to TOAST). The map-maker’s noise model was estimated using power spectra from observations of faint dust emission in the constellation Puppis (map centered at $l = 239^{\circ}0$, $b = -1^{\circ}7$), with simulated astrophysical signal subtracted. The noise model is consistent with white noise plus $(1/f)^{\alpha}$ correlations that level out at low frequency due to data preprocessing. Correlations between detectors and non-stationarity of the noise were not required by the model. Instrumental polarization (Section 3.3) was removed as per Matthews et al. (2014). Per-pixel covariance matrices for Stokes I , Q , and U were estimated as the 3×3 diagonal block of the full pixel-pixel covariance matrix. Noise-only maps, both simulations and null tests (see Section 3.6), are consistent with the estimated covariances, up to a constant scaling factor due to unmodeled noise. A pixel size of $10''$ was used for all signal and covariance maps.

3.5. Diffuse Emission Subtraction

To study the polarization properties and magnetic field morphology of Vela C it is necessary to isolate polarized dust emission originating in Vela C from the diffuse polarized emission associated with Galactic foreground and background dust as well as the Vela Molecular Ridge.²⁸ This separation requires extra care as previous studies show that diffuse sightlines, which may be used to estimate the foreground/background polarized emission, tend to have a higher average polarization fraction than dense cloud sightlines. In particular, *Planck* observations show that in the more diffuse clouds there is a range of p values with the maximum reaching 15%–20%, while such high values are not seen in the higher column density clouds (e.g., Orion, Ophiuchus, Taurus), where the average p is consistently lower (Planck Collaboration Int. XX 2015). Polarized emission from diffuse dust along dense cloud sightlines could therefore contribute significantly to the overall polarization measured. In this section we present two different diffuse emission subtraction methods, one conservative and one more aggressive with respect to diffuse emission removal.

In the conservative method for diffuse emission subtraction, we considered most of the emission surrounding Vela C as defined by Hill et al. (2011) to be associated with the cloud. The Hill et al. (2011) Vela C cloud subregions are overplotted (solid white lines) on a map of $500 \mu\text{m}$ total intensity in Figure 1. The zero-point for the intensity of the cloud emission was set by specifying a region with relatively low intensity near Vela C and assuming that emission in this reference region also contributes to sightlines on the cloud with spatial uniformity. This low flux region is labeled “C” in Figure 1. We calculated the average Stokes I , Q , and U in that region, and the appropriate mean flux was then subtracted from each of the maps. The result was a set of maps of Vela C emission isolated from the Galaxy, assuming a minimal, uniform contribution from foreground and background emission.

In the aggressive method we considered most of the diffuse emission surrounding Vela C to be unassociated with the cloud, and accordingly a higher level of flux needed to be removed to isolate the cloud. Furthermore, we noted that there is

significantly more emission to the south of Vela C than to the north; thus it is reasonable to assume that the true map of the region consists of the Vela C cloud superimposed on a varying Galactic emission profile. In this method of referencing, we defined two regions closely surrounding the cloud (marked “A1” and “A2” in Figure 1) and performed two-dimensional linear-plane fits to the Stokes I , Q , and U maps excluding all map pixels except those located in regions A1 and A2. The three free parameters in these fits were the linear slopes of the plane in the directions tangent to l and b and a map offset. The equations for each of the resulting plane-fits to the I , Q , and U maps were used to specify the intensity to be subtracted from each pixel in the maps. Note that for regions far from Vela C, the linear approximation of the Galactic emission profile breaks down, leading to an inappropriate extrapolation. Therefore we defined an area within which the linear fit referencing method is valid (blue quadrilateral in Figure 1), bounded on the north and south by the reference regions A1 and A2, and on the east and west by the edges of the well-sampled portion of the map. This “validity” area roughly coincides with the four southernmost regions of Hill et al. (2011). We note that some of the emission in A1 and A2 might in fact be associated with Vela C, so this method is likely to over-subtract the diffuse dust emission.

The true I , Q , and U maps of Vela C probably exist somewhere between our most extreme physically reasonable assumptions corresponding to the conservative and aggressive diffuse emission subtraction methods. In this paper we present results for an “intermediate” diffuse emission subtraction method, derived by taking the arithmetic mean of the I , Q , and U maps from the aggressive and conservative methods. Most of our analyses are then repeated using the aggressive and conservative methods as a gauge of the uncertainties associated with the diffuse emission subtraction.

3.6. Null Tests

To characterize possible systematic errors in our data, we performed a series of null tests, which are described in detail in Appendix A. In these, we split the $250 \mu\text{m}$ observations²⁹ into two mutually exclusive sets. If the polarization parameters from the two independent data sets agree, we can conclude that the impact of systematics is small, and the uncertainties are properly characterized by Gaussian errors produced by TOAST. The four methods of splitting are: data from the left half of the array versus the right half; data from the top half of the array versus the bottom half; data from earlier in the flight versus later in the flight; and alternating every other scan set sequentially throughout the flight.

For each null test we made separate maps of I , Q , and U , which were then used to calculate residual maps of the polarized intensity P , the polarization fraction p , and the polarization-angle ψ as described in Appendix A. (The quantities P , p , and ψ are defined in Appendix B). If our data had no systematic errors we would expect to see uncorrelated noise in the residual maps. For P and p if the residuals were less than one-third of the signal in a given map pixel then that pixel was said to pass the null test. For ψ the residuals had to be less than 10° to pass the null test. We examined each of the four null tests listed above for each of the two methods of

²⁸ It should also be noted that observations made by BLASTPol are inherently differential measurements, and thus the map zero-intensity level is uncertain.

²⁹ As discussed in Appendix A the BLASTPol $250 \mu\text{m}$ observations of Vela C are better suited than the $500 \mu\text{m}$ data for performing null tests.

diffuse emission subtraction (Section 3.5) in P , p and ψ giving a total of 24 checks that our measured polarization signal is significantly above the systematic uncertainty level.

We found that our map passed these tests for the majority of sightlines inside the “cloud” region shown in Figure 1 (blue solid line). The exceptions occurred in regions where the fractional polarization was small, so that a comparison of the scale of the polarization signal to the scale set by residuals in the null tests resulted in an apparent failure. The fact that we saw null test failures correlating with low p , but not with absolute difference in the null test I maps led us to the interpretation that the apparent low signal level compared to the null test residual is due to decreased signal and not increased systematic uncertainties. We did see significant structure in the null test residual maps of Q and U near the compact H II region RCW 36, which coincided with null test residuals of one-fourth p , though the residuals in ψ were much smaller than 10° . These p measurements technically pass the null test criteria, but the systematic errors are larger than the statistical errors. We conclude that for the validity region shown in Figure 1 the null tests are passed, with the exception of a circular area centered on RCW 36 ($l = 265^\circ.15$, $b = 1^\circ.42$ within a radius of $4'$).

4. BLAST-POL POLARIZATION MAPS

In this section we present maps of the Stokes parameters I , Q , and U , linearly polarized intensity (P), and polarization fraction ($p = P/I$). The polarization descriptors and covariances used in our analysis are summarized in Appendix B. We also present maps of Φ , the inferred orientation of magnetic field projected onto the plane of the sky, which is assumed to be the orientation of the polarization of the dust emission (described by ψ) rotated by 90° , and the localized dispersion in the polarization-angle (S).

Because p and P are constrained to be positive any noise in the Q and U maps will tend to increase the measured polarization. Accordingly, we crudely debias p and P according to

$$p_{db} = \sqrt{p^2 - \sigma_p^2}, \quad (1)$$

and

$$P_{db} = \sqrt{P^2 - \sigma_p^2}, \quad (2)$$

(Wardle & Kronberg 1974). This method of debiasing is appropriate only where σ_p is small compared with p (Montier et al. 2015). We note that the median value of p/σ_p in our map is ~ 25 , so for most of our map this debiasing method is applicable.

4.1. Diffuse Emission Subtracted Maps of I , Q , and U , and Derived Maps of P , and p

Figure 3 shows Vela C $500 \mu\text{m}$ maps for the three Stokes parameters I , Q , and U . The maps have been smoothed to 2.5 resolution, as described in Section 3.2, and use the intermediate diffuse emission subtraction method (Section 3.5). Overlaid in gray are the outlines of the subregions of Vela C as defined in Hill et al. (2011) and labelled in Figure 8. The BLASTPol I map peaks at the location of RCW 36.

Also included in Figure 3 is the derived map of the polarized intensity (P), which generally shows some signal where there is cloud emission. However, the correspondence is certainly not perfect, and varies considerably across the map. For example, along most of the Center-Ridge there is a corresponding peak

in the P map along the main ridge. In the South-Ridge there are peaks at similar locations in the P and I maps. But in the South-Nest, prominent areas of polarized emission are only seen around the edge of the cloud structure seen in I . There are also some regions of significant P that stand out less in I , for example, along the north edge of the Center-Ridge.

Figure 4 shows the polarization fraction ($p = P/I$) for each of the three different diffuse emission subtraction choices discussed in Section 3.5. The conservative diffuse emission subtraction (top panel) results in p that is lower on average than from the aggressive diffuse emission subtraction (middle panel). This is expected as p is commonly observed to increase for regions of low dust emission. Thus, compared to the aggressive subtraction method that uses regions closer to the cloud with lower average p , the conservative method removes more P relative to I . The bottom panel shows the p map resulting from the intermediate diffuse emission subtraction method. Unless otherwise specified, for the remainder of the paper p , ψ , and Φ are calculated from Stokes parameter maps using the intermediate diffuse emission subtraction method.

The mean value of p in our map is 6.0% with a median of 3.4%. For the map pixels within the dense cloud subregions defined by Hill et al. (2011) the mean polarization fraction is 3.5% with a median of 3.0% and a standard deviation of 2.4%. Previous submillimeter polarization maps having spatial coverage corresponding to the scales of entire clouds have yielded roughly similar values. Specifically, after subtracting the background/foreground emission, Planck Collaboration Int. XXXIII (2016) found mean $850 \mu\text{m}$ polarization fractions of 1.8%, 5.0%, and 6.1% for three nearby molecular clouds, while $450 \mu\text{m}$ polarization maps of four GMCs made by Li et al. (2006) with SPARO at the South Pole yield a mean polarization fraction of 2.0%. Our p map shows behavior that is broadly consistent with expectations from the P map. Values of p tend to decrease with increasing I , but there is not a one-to-one anticorrelation between p and I .

4.2. Inferred Magnetic Field Direction

Figure 5 shows a detailed view of the magnetic field orientation projected onto the plane of the sky Φ , as inferred from the BLASTPol $500 \mu\text{m}$ data. This figure uses a “drapery” pattern produced using the line integral convolution method of Cabral & Leedom (1993) superimposed on the BLASTPol $500 \mu\text{m}$ I map.³⁰ Dotson (1996) showed that there is significant ambiguity in inferring the magnetic field lines from polarization data, particularly as polarization maps can sample multiple cloud structures along the line of sight, each potentially having a different magnetic field orientation. The drapery image is presented solely to show the range of orientations of Φ , and to give a sense of the range of spatial scales probed by BLASTPol. Figure 6 shows Φ as a series of line segments (approximately one line segment per 2.5 BLASTPol beam).

The projected cloud magnetic field direction appears to change across Vela C: at low Galactic latitudes the field is mostly perpendicular to the main cloud elongation direction, while at higher Galactic latitudes it bends to run mostly parallel to the cloud elongation direction. We also see some sharp

³⁰ This visualization is produced with the same code used in Planck Collaboration Int. XXXV (2016) and will be further discussed in a forthcoming paper by D. Falceta-Gonçalves et al.

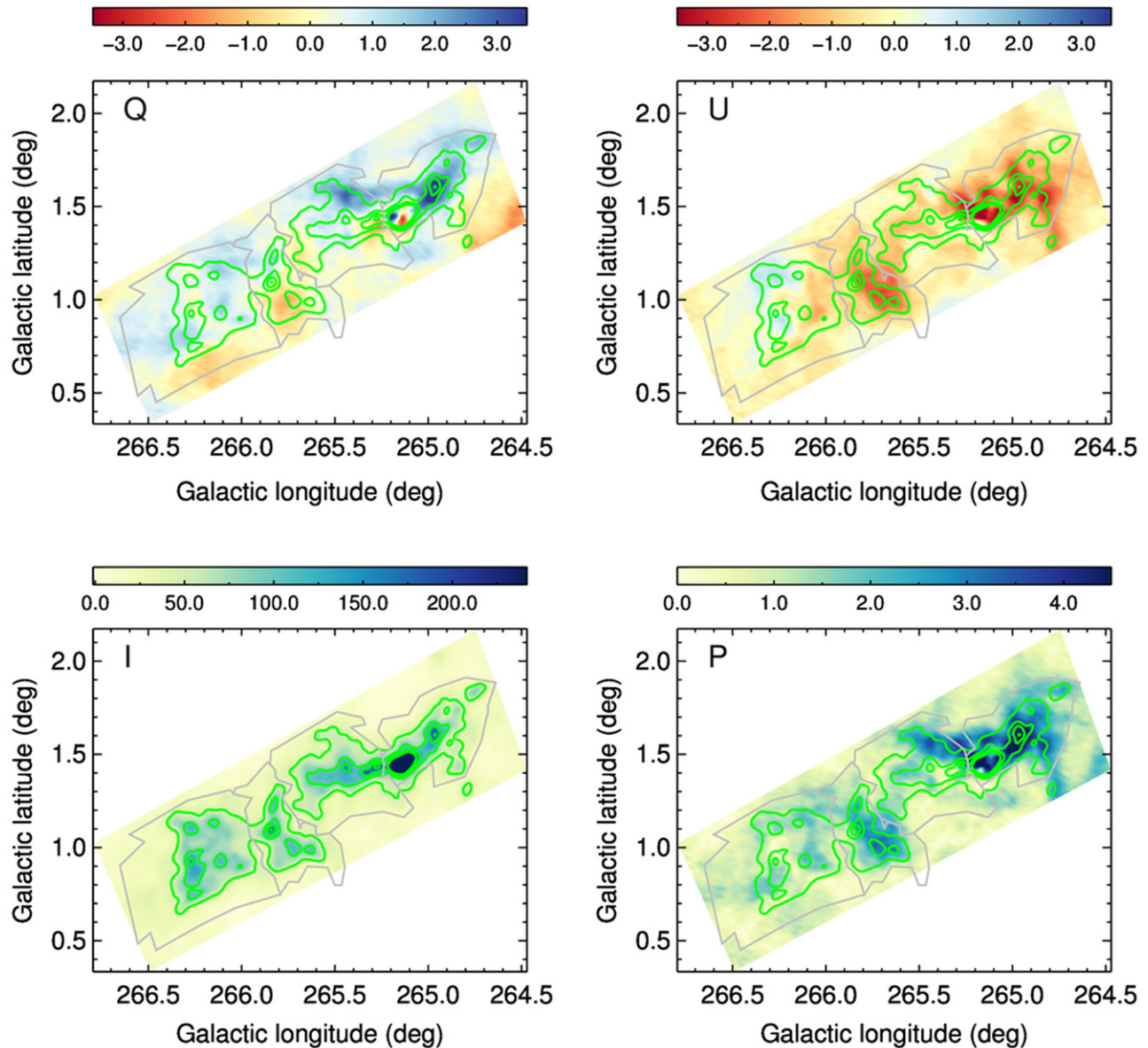


Figure 3. BLASTPol 500 μm Vela C maps of I , Q , U , and the total polarized intensity P (which is debiased as described in Section 4). The color scale units are MJy sr^{-1} . Contours indicate I levels of 46, 94, 142, and 190 MJy sr^{-1} , and the gray outlines indicate cloud subregions covered by our observations as in Figure 1.

changes in Φ , most noticeably in the South-Nest, and near the compact H II region RCW 36.

Figure 7 shows that the dispersion in magnetic field orientation across the Vela C cloud is 28° . Novak et al. (2009) calculated dispersions on similar spatial scales by combining the large-scale GMC polarization maps of Li et al. (2006) with higher angular resolution submillimeter polarimetry data. They obtained 27° – 28° , nearly the same result. In future publications we will present statistical studies of the correlations between magnetic field orientation, filamentary structure, and cloud velocity structure.

4.3. Polarization Angle Dispersion Function

To quantify the disorder of Φ in our Vela C maps at small scales we calculate the polarization-angle dispersion function S , implementing the formalism described in Section 3.3 of Planck Collaboration Int. XIX (2015). For each pixel in our map, S is defined as the rms deviation of the polarization-angle $\psi(\mathbf{x})$ for

a series of points on an annulus of radius δ :

$$S^2(\mathbf{x}, \delta) = \frac{1}{N} \sum_{i=0}^N S_{xi}^2, \quad (3)$$

where δ is the length scale of the dispersion, \mathbf{x} is the position for which we evaluate the polarization-angle dispersion and

$$S_{xi} = \psi(\mathbf{x}) - \psi(\mathbf{x} + \delta_i). \quad (4)$$

Because S is always positive it is biased due to noise. We debias using the standard formula

$$S_{db}^2(\delta) = S^2(\delta) - \sigma_S^2, \quad (5)$$

where σ_S^2 is the variance of S .

Figure 6 shows S for $\delta = 2/5$ (~ 0.5 pc), the smallest scale that can be resolved with our smoothed beam. (Hereafter we refer to $S(2/5)$ as S). The most striking features in the S map correspond to regions of sharp changes in Φ , which is indicated with line segments. These high dispersion regions sometimes

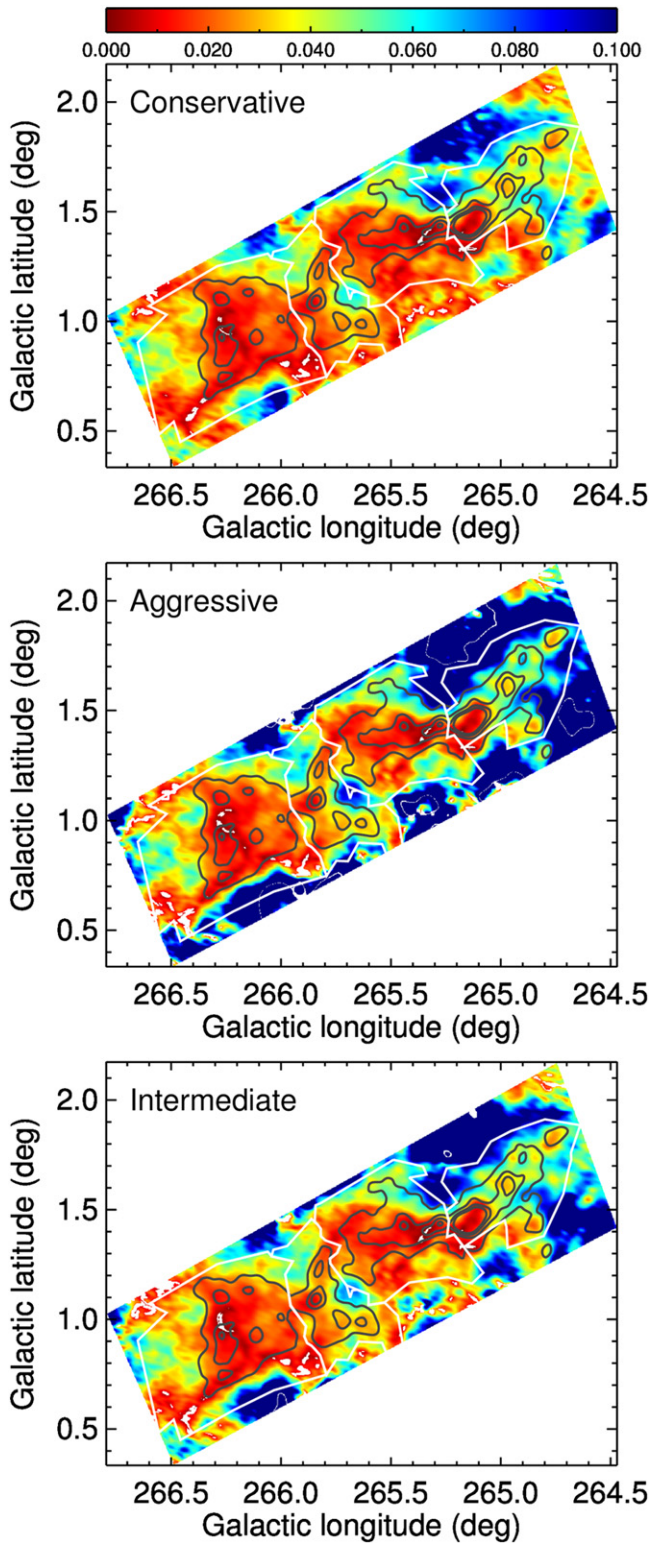


Figure 4. BLASTPol $500\ \mu\text{m}$ maps of p obtained using different methods for separating the polarized emission of Vela C from that of diffuse background/foreground dust (Section 3.5): conservative method (top panel); aggressive method (middle panel), and intermediate method (bottom panel). Only sightlines where $p > 3\sigma_p$ and $I > 0$ are shown. The p maps shown have been debiased using the methods described in Section 4. Gray contours indicate I levels of 46, 94, 142, and 190 MJy sr^{-1} , and the white outlines indicate the four Vela C cloud subregions as in Figures 1 and 8.

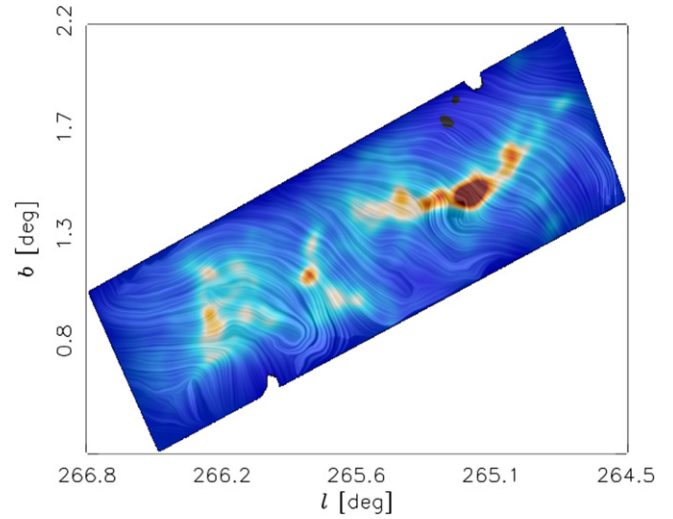


Figure 5. BLASTPol $500\ \mu\text{m}$ I map with the inferred plane of the sky magnetic field component (Φ) overlaid as a “drapery” image (only regions where $I > 0$ are shown). The drapery pattern is produced using the line integral convolution method (Cabral & Leedom 1993) and indicates the orientation of the magnetic field as projected on the plane of the sky. Note that this drapery pattern was made from all of the Φ data with no masking of sightlines having large uncertainties in Φ . This image is meant to show the level of detail available in the BLASTPol Φ maps, but should not be used for quantitative analysis.

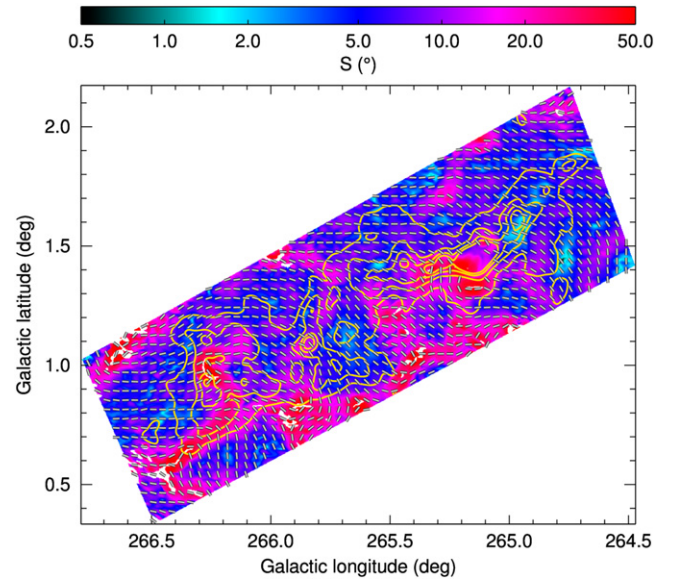


Figure 6. BLASTPol $500\ \mu\text{m}$ map of the dispersion in the polarization-angle (S) in degrees on $0.5\ \text{pc}$ scales ($\delta = 2''.5$) as defined in Section 4.3. The S map is shown where $S > 3\sigma_S$. Line segments show the orientation of the magnetic field as projected on the plane of the sky (Φ), derived from the BLASTPol $500\ \mu\text{m}$ data. The Φ measurements are shown approximately every $2''.5$. Contours indicate $500\ \mu\text{m}$ I intensity levels of 46, 94, 142, and 190 MJy sr^{-1} .

occur near the locations of dense filaments (for example, the sharp bend in the South-Nest). More often they correspond to sightlines of lower than average p and do not appear to be coincident with any prominent cloud feature in I .

4.4. Polarization Map Sampling and Sightline Selection

Our BLASTPol polarization maps were calculated from Stokes parameters smoothed to a resolution of $\sim 2''.5$ as discussed in Section 3.2. The resulting polarization maps were

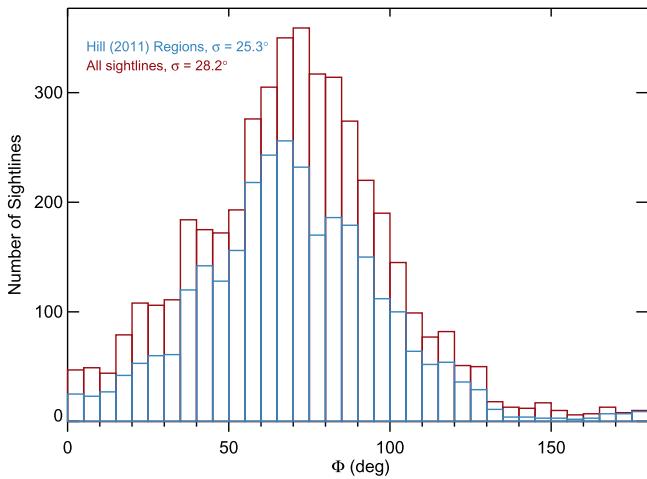


Figure 7. Histograms of the BLASTPol 500 μm inferred magnetic field direction Φ for all Vela C sightlines (red) and sightlines lying inside the Hill et al. (2011) subregions (blue). Sightlines included in these histograms have $\sigma_\Phi < 10^\circ$ and both $|\psi_{\text{int}} - \psi_{\text{con}}| < 10^\circ$ and $|\psi_{\text{int}} - \psi_{\text{agg}}| < 10^\circ$ (see Section 4.4). The standard deviation of each distribution is given at upper-left.

then sampled every $70''$ to ensure at least Nyquist sampling. In total there are 4708 projected magnetic field sightlines over the validity region defined in Section 3.5.

In the following sections we attempt to model the polarization fraction p as a function of N , T , and S . For these detailed studies we restrict our analysis to sightlines that encompass the dense cloud regions as defined by Hill et al. (2011). These sightlines are better probes of the polarization structure in the cloud and are less sensitive to systematic uncertainties in our ability to separate the polarized emission emitted by diffuse dust foregrounds/backgrounds from the polarized emission emitted by dust grains in Vela C.

To ensure a robust sample, we use only p values that are large enough to be unaffected by uncertainties in instrumental polarization removal ($p > 0.1\%$, see Section 3.3), and for which we have at least a 3σ detection of polarization ($p > 3\sigma_p$), which corresponds to an uncertainty in the polarization angle $\sigma_\psi < 10^\circ$. To ensure that the polarization values are not dependent on our choice of diffuse emission subtraction method we require that $p_{\text{int}} > 3|p_{\text{int}} - p_{\text{con}}|$ and $p_{\text{int}} > 3|p_{\text{int}} - p_{\text{agg}}|$, where p_{con} , p_{agg} , and p_{int} are the polarization fraction values calculated using the conservative, aggressive, and intermediate diffuse emission subtraction methods respectively (see Section 3.5). Similarly, we require that $|\psi_{\text{int}} - \psi_{\text{con}}| < 10^\circ$ and $|\psi_{\text{int}} - \psi_{\text{agg}}| < 10^\circ$. We also exclude sightlines from a $4'$ radius region near RCW 36 as these show residual structure in our null tests (see Section 3.6). In total 2488 out of a 3056 possible Hill et al. (2011) sightlines meet these criteria. For our analysis of p versus N , T , and S in Sections 6 and 7 we also require at least $3\text{-}\sigma$ measurements of N , T , and S where the errors on N and T are derived from the SED fit covariance matrices (see Section 5). This results in a final sample of 2378 sightlines.

5. COLUMN DENSITY AND TEMPERATURE MAPS DERIVED FROM HERSCHEL SPIRE AND PACS DATA

To derive column density and dust temperature maps we used publicly available *Herschel* SPIRE and PACS data.

SPIRE uses nearly identical filters to BLASTPol, but has higher spatial resolution (FWHM of $17''.6$, $23''.9$, and $35''.2$ for the 250, 350, and 500 μm bands, respectively). Data taken with the PACS instrument in a band centered at 160 μm (FWHM of $13''.6$) were used to provide additional sensitivity to warm dust. *Herschel* maps were generated using Scanamorphos (Roussel 2013) and additional reduction and manipulation was performed in the *Herschel* Interactive Processing Environment (HIPE version 11) including the Zero Point Correction function for the SPIRE maps. The resulting *Herschel* maps were smoothed to $35''.2$ resolution by convolving with Gaussian kernels of an appropriate size and then regridding to match the 500 μm map.

Similar to the diffuse emission subtraction described in Section 3.5, we attempted to separate the Galactic foreground and background dust emission from the emission of Vela C. As the regions used to define the diffuse emission subtraction in Section 3.5 were not covered by the *Herschel* map we defined four alternate “diffuse emission regions” (see Figure 8 top panel). These regions were presumed to contain little emission from dust in Vela C and thus they are reasonable representations of the contribution due to diffuse dust emission. For the initial analysis described below, the mean intensity in Region 1 was subtracted from each of the 160, 250, 350, and 500 μm maps, and the maps were then further smoothed to match the $2''.5$ resolution of the BLASTPol maps.

Modified blackbody SED fits were made for each map pixel using the methods described in Hill et al. (2009, 2010, 2011) and using the dust opacity law of Hildebrand (1983) with a dust spectral index $\beta = 2$. The resulting column density (N) and dust temperature (T) maps are shown in Figure 8 (middle and bottom panels, respectively). It should be noted that above a temperature of ~ 20 K, the dust emission is expected to peak at wavelengths shorter than 160 μm . For these warmest sightlines our estimates will have a higher degree of uncertainty. The derived N and T maps were visually compared to the higher resolution column density and temperature maps from Hill et al. (2011), which did not include a diffuse emission subtraction. Our maps are in close agreement with the Hill et al. (2011) maps for column density sightlines where Vela C emission is strong compared to the diffuse emission component. Note that we computed maps of the column density of hydrogen nuclei while Hill et al. (2011) calculated the column density of H_2 .

Much of the analysis in the present paper focuses on comparisons between parameters such as polarization fraction p , N , and T . From Figure 8 we see that N and T are strongly anti-correlated. Similar trends were noted by Palmeirim et al. (2013) in their *Herschel* study of a cold cloud in Taurus. We interpret this as a result of radiation shielding in the densest parts of the cloud. This interpretation can be tested by examining a plot of 250 μm intensity versus 500 μm intensity, as shown in Figure 9. In this figure there is a noticeable bend in the otherwise linear relationship between the two intensities. Since submillimeter dust emission in molecular clouds is typically optically thin, larger intensity at either wavelength corresponds to higher column density. However, beyond the bend we notice that the slope of the 500 μm intensity versus 250 μm intensity relation decreases. The simplest explanation is that the dust in denser regions of the cloud is colder, due to radiation shielding.

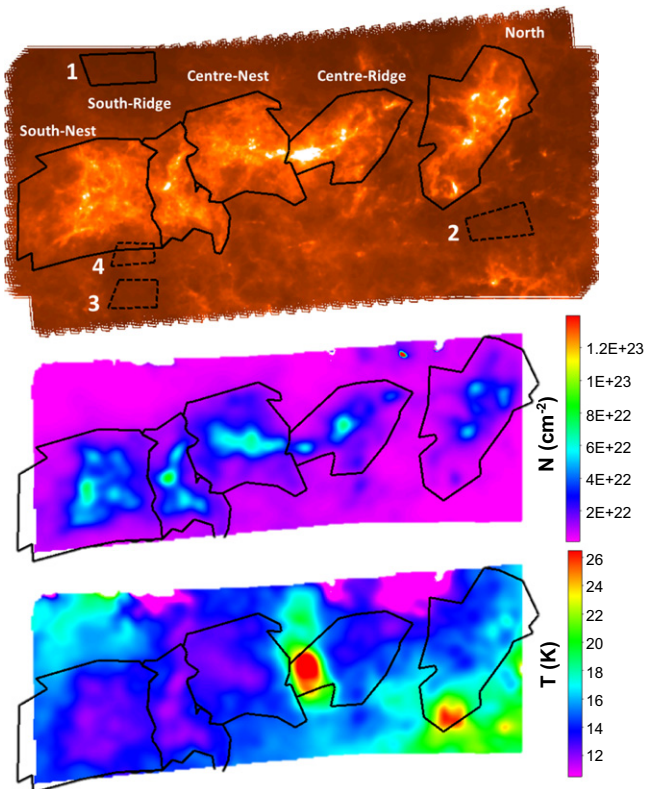


Figure 8. *Herschel* Vela C 500 μm intensity (top panel, FWHM = $35''$), column density (N , middle panel, FWHM = $2''.5$), and dust temperature (T , bottom panel, FWHM = $2''.5$). The N and T maps were derived from *Herschel* data using the methods described in Section 5. Numbered quadrilaterals correspond to different diffuse emission regions for which the average intensity is indicated in Figure 9. Note that the mean intensity in Region 1 was subtracted from each of the 160, 250, 350, and 500 μm maps before SED fitting. The solid black polygons (labeled in the top panel) correspond to the cloud subregions as defined in Hill et al. (2011). From left to right these are: the South-Nest, a region of many overlapping filaments; the South-Ridge, dominated by a single dense filament; the Center-Nest; and Center-Ridge, which contains the ionizing source(s) powering the compact H II region associated with RCW 36. Hill et al. (2011) also include an additional region, designated North, that was not covered in the deep BLASTPol survey of Vela C.

An alternative interpretation of the bend seen in Figure 9 is to hypothesize a uniformly cold cloud spatially superimposed on diffuse emission from warmer dust. To explore this possibility we examined the location of each diffuse region on Figure 9 relative to the bend in the observed curve of 250 μm versus 500 μm intensity. Subtracting the diffuse emission flux essentially sets a new origin for this graph and is equivalent to the diffuse emission subtraction discussed in Section 3.5, leaving only emission from dust grains in the Vela C cloud. As can be seen from Figure 9, the diffuse emission regions, even very aggressively placed ones, reposition the origin to locations significantly below the bend in the curve, indicating that the observed T and N anticorrelation is intrinsic to the Vela C molecular cloud. As a further check the SED fits described above were redone using diffuse emission Regions 2, 3, and 4 as the reference regions, instead of using Region 1 (see Figure 8). The corresponding N maps are very similar to the one shown in Figure 8, especially for the densest regions.

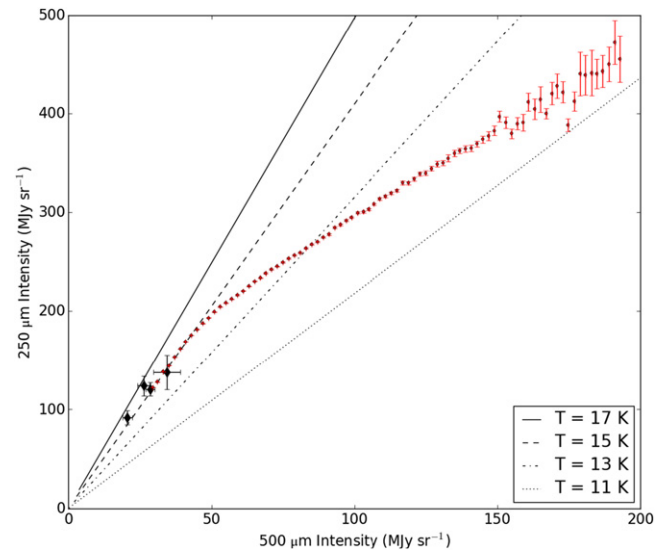


Figure 9. Median values of *Herschel* 250 μm intensity in bins of *Herschel* 500 μm intensity for the South-Nest region in Vela C (as labeled in Figure 8). The error bars correspond to the standard deviation of the 250 μm intensity values in each bin. Black lines correspond to the expected intensity ratios for uniform temperature dust. Diamonds indicate the average 250 and 500 μm intensities for the four numbered diffuse emission regions indicated in the top panel of Figure 8 (from left to right these indicate regions 1, 2, 3, and 4). Error bars show the standard deviation of intensity values in each region.

6. DEPENDENCE OF POLARIZATION FRACTION ON N AND T

Before considering the polarization fraction p , we first attempt to separate sightlines that show significant heating from sources internal to Vela C from sightlines that appear to be predominantly heated by the interstellar radiation field (ISRF). The polarization properties of sightlines near a source of intense radiation, such as the compact H II region RCW 36 in Vela C, might differ from the polarization properties of cloud sightlines where star formation is at an earlier stage. The presence of a bright radiation source might affect the efficiency of RATs in aligning dust grains with respect to the local magnetic field. Also, the presence of expanding ionized gas in H II regions can alter the magnetic field geometry, for example as seen in SPARO observations of the Carina Nebula (Li et al. 2006).

Figure 10 shows T versus $\log N$ for sightlines selected as discussed in Section 4.4. (Note that throughout this paper \log refers to \log_{10} .) As discussed in Section 5 the ISRF can more easily penetrate sightlines of low column and therefore average temperatures of low N sightlines tend to be higher. Figure 10 generally shows decreasing T with increasing $\log N$, however it also shows that a minority of sightlines have temperatures lying well above this approximately linear trend. We fit the equation $T = a \log N + b$, using Chauvenet's criterion (Chauvenet 1863) iteratively to remove outliers (diamonds in Figure 10). The 143 sightlines rejected as outliers are located near the compact H II region RCW 36 (upper panel of Figure 11). These sightlines appear to be heated by the H II region, yielding temperatures lying above the trend seen for ISRF heated sightlines.

Figure 12 shows the dependence of p on N and T for ISRF-heated sightlines (left side, top and middle panels respectively). In general p decreases with increasing N and increases with

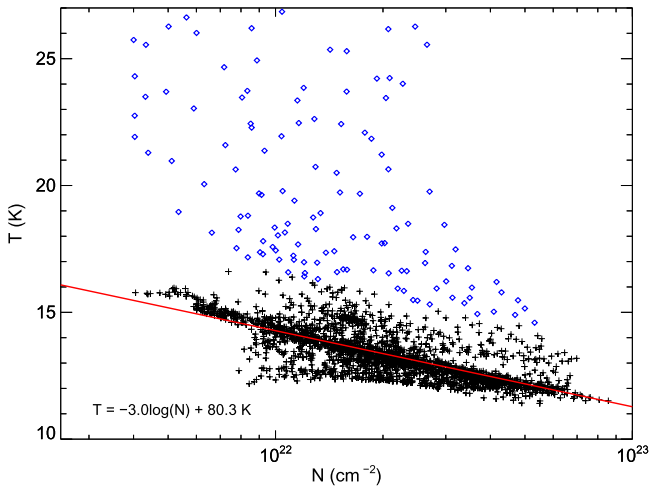


Figure 10. Dust temperature (T) vs. $\log N$ for all Vela C sightlines in the subregions defined by Hill et al. (2011). Blue diamonds show sightlines that were rejected by an iterative application of Chauvenet’s criterion. These 143 sightlines appear to be heated by the compact H II region RCW 36. The other 2235 sightlines (crosses) appear to be heated only by the interstellar radiation field (ISRF). The red line corresponds a fit to all ISRF-heated sightlines, as described in Section 6.

increasing T . To quantify the dependence of p on N we fit a model of the form

$$p = CN^{\alpha_N} \quad (6)$$

where, C and α_N are constants. This is equivalent to a linear fit in logarithmic space

$$\log p = \alpha_N \log N + C. \quad (7)$$

Via a fit to Equation (7), we find that $\alpha_N = -0.58 \pm 0.02$. Each measurement of $\log p$ is given equal weight in our fit. By giving each data point equal weight (equal fractional error in p) we are assuming that the deviations of the $\log p$ data points from the fit described in Equation (7) are caused by additional dependences of p on other quantities, rather than uncertainties in our measurements of $\log p$. This assumption is reasonable, because our polarization measurement uncertainties are generally quite small. For example, the median signal-to-noise of our p measurements is 36, and the median signal-to-noise of the N measurements for these same sightlines is even higher. The uncertainties on our fitted parameters are calculated using the bootstrapping method with replacement (Press et al. 1992), repeating the fits for each of 10,000 random selections. The standard deviation of the derived power-law exponents is used as an estimate of their uncertainty.

Similarly, for p versus T (Figure 12 middle left panel), we fit to the relation $\log p = \beta_T T + c_1$, and find that $\beta_T = 0.125 \pm 0.005$, which implies that $p \propto \exp(0.29T)$. However, Figure 10 shows that N and T are highly correlated for ISRF heated sightlines. We can remove the correlation of p with N by computing:

$$p_i^{[N]} = p_i \left(\frac{\bar{N}}{N_i} \right)^{\alpha_N}, \quad (8)$$

where $p_i^{[N]}$, p_i , and N_i are the i th decorrelated p measurement, and original p and N measurements, respectively, and \bar{N} is the median value of N for our sightlines. The bottom left panel of

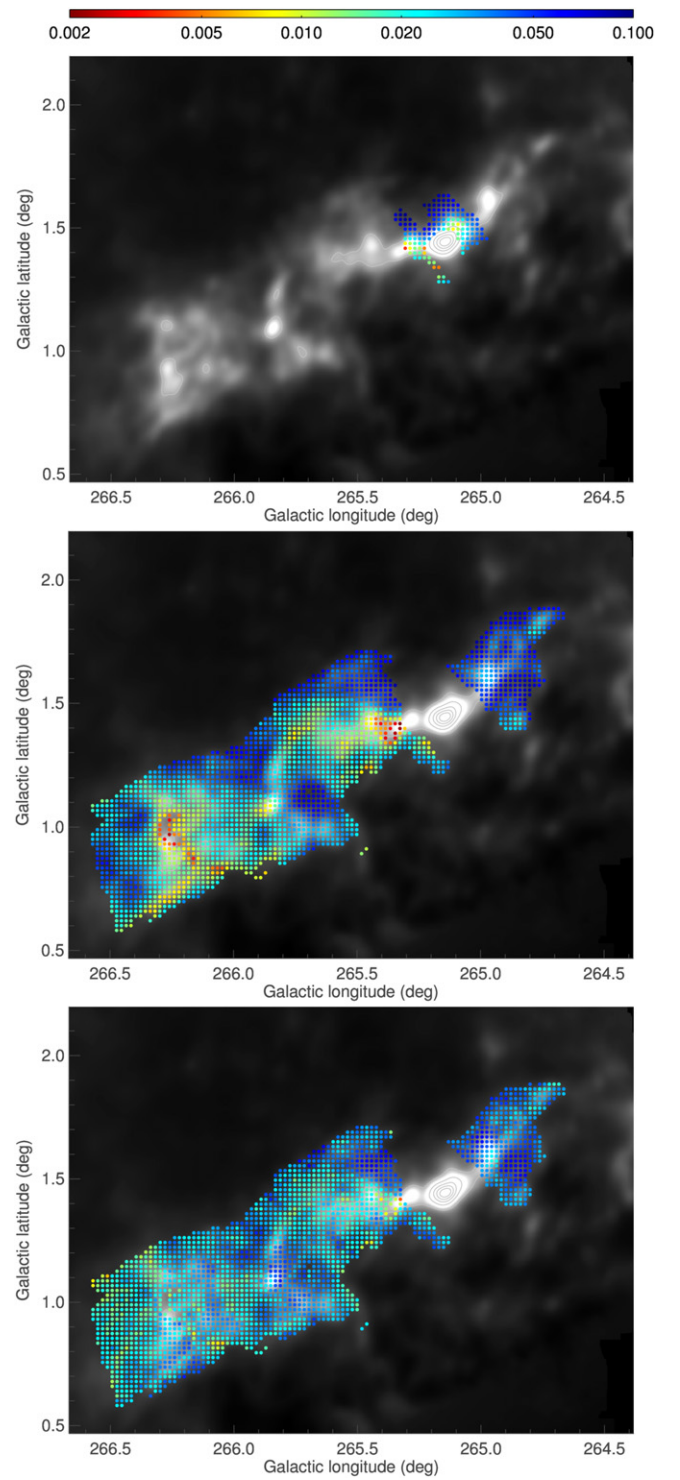


Figure 11. Color-coded plot of p over the range of 0.002 to 0.100 for all RCW 36 heated (top panel) and ISRF heated (middle panel) BLASTPol sightlines that pass the criteria described in Section 4.4. The bottom panel shows $p^{[N,S]}$, which is p for the ISRF heated sightlines decorrelated from N and S using Equation (11) in Section 7.2. If Equation (10) accounted for the entire variation of p , then the value of $p^{[N,S]}$ would be constant at 0.029. The background image is I_{500} .

Figure 12 shows $p^{[N]}$ versus T . By removing the anticorrelation of p with N , we also remove any correlation with T . Thus it appears that there is no correlation between p and T that is independent of the correlation between p and N .

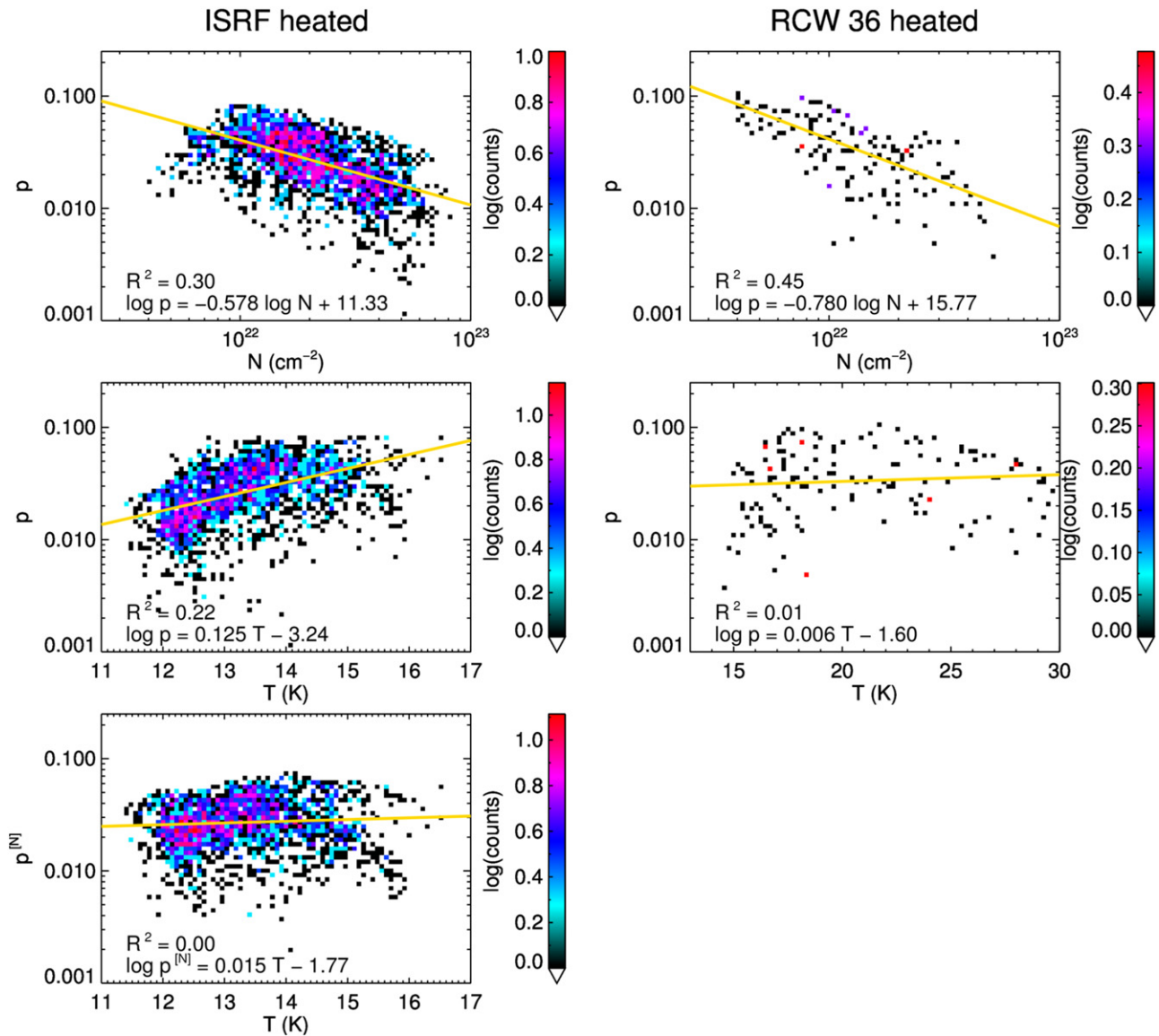


Figure 12. Two-dimensional histograms showing the correlations between p , N , and T for ISRF-heated sightlines (left) and sightlines that show evidence of heating from RCW 36 (right). The correlations shown are: polarization fraction (p) vs. column density (N) (top panels); p vs. dust temperature (T) (middle panels); and $p^{|N|}$, the polarization fraction with the dependence on column density removed using Equation (8) vs. T (bottom left panel). All data points used to make these plots passed the selection criteria described in 4.4. The color of each pixel is proportional to the logarithm of the number of data points located within the pixel. The solid lines show fits to the data (Section 6). The best-fit equations are listed on each plot in addition to the coefficient of determination (R^2).

For the sightlines that show significant heating from RCW 36 we see a similar decrease in p with increasing N and find a power-law exponent of $\alpha_N = -0.78 \pm 0.06$ (Figure 12 top right panel). However, for these sightlines there is no apparent correlation between p and T (Figure 12 middle right panel).

7. DEPENDENCE OF POLARIZATION FRACTION ON N AND S

In this section our goal is to build an empirical model for the dependence of p on N and the polarization-angle dispersion on $2/5$ (0.5 pc) scales S , for an early stage star-forming region. Therefore we only consider ISRF-heated sightlines. Additionally, we do not include T as a parameter of the empirical model as it was shown in Section 6 that the p versus N and p versus T correlations are degenerate. We choose N rather

than T as our independent variable because the most natural explanation for the N versus T anticorrelation for ISRF-heated sightlines is that the density structure of the cloud determines the average temperature of the sightlines, rather than T determining N .

7.1. Individual Correlations Among p , N , and S

Figure 13 shows the median p (color map) for bins of S and N for ISRF-heated sightlines. There is a clear decrease of p with increasing N and S . Individual correlations are shown in Figures 12 and 14, and the derived associated power-law exponents are listed in Table 1.

Decreasing p with increasing N has been seen in submillimeter polarization observations of many clouds and cores (e.g., Matthews et al. 2001; Li et al. 2006). The observed decrease in p is often attributed to either cancellation of polarization signal

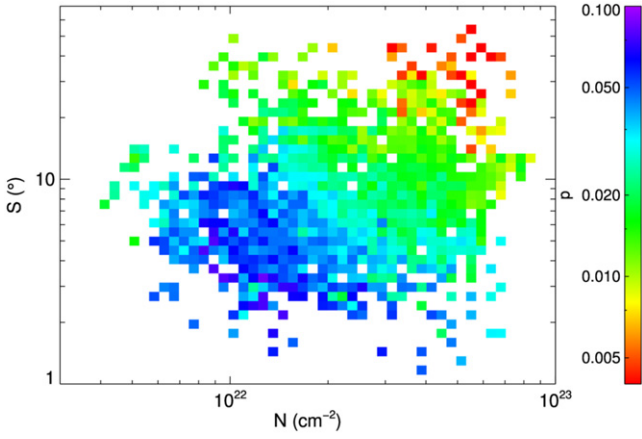


Figure 13. Median p color-coded in bins of S and N for all ISRF-heated sightlines. The use of logarithmic scales for p , N , and S brings out the systematic relationship suggestive of power-laws.

for high- N sightlines due to more disorder in the magnetic field, or to changes in grain alignment efficiency within the cloud. These possible explanations are discussed further in Section 8.

In Section 4.3, we showed that Vela C has high values of S in localized filament-like regions, where there are sharp changes in magnetic field direction. High S depends implicitly on spatial changes in the magnetic field locally in the map, and any related changes in the magnetic field direction within the volume sampled by the BLASTPol beam could lead to lower p . The top panel of Figure 14 shows p versus S . There is a clear anticorrelation between p and S ($\alpha_S = -0.67 \pm 0.02$, the coefficient of determination $R^2 = 0.47$). We see no dependence of S on N (Figure 14, lower panel).

We showed in Section 6 that the dependence of p on N can be removed using Equation (8) to create $p^{[N]}$. Similarly we can normalize out the dependence of p on S by calculating

$$p_i^{[S]} = p_i \left(\frac{\bar{S}}{S_i} \right)^{\alpha_S}. \quad (9)$$

The top panel of Figure 15 shows that by removing the dependence of S from p the degree of correlation of $p^{[S]}$ with N increases ($R^2 = 0.35$ compared to 0.30). Similarly, the bottom panel shows that the correlation of $p^{[N]}$ with S is better than the correlation of p with S ($R^2 = 0.50$ compared to 0.47). This indicates that both N and S contribute independently to the structure seen in p . The fitted power-law exponents tend to be systematically shallower for the decorrelated $p^{[S]}$ and $p^{[N]}$ than for trends with p (see the first row of Table 1), which might imply a weak underlying correlation between N and S (see Figure 14, bottom panel).

7.2. Power-law Fit $p(N, S)$

As noted in Section 7.1, Figure 13 shows a color map of the median p binned two-dimensionally in S and N for ISRF-heated sightlines. The clear decrease of p with both increasing N and S is suggestive of a joint power-law relationship. Here we derive a function $p(N, S)$ that accounts for most of the structure seen in the p map. Specifically, we adopt the joint power-law form

$$\log p(N, S) = K + \alpha_N \log N + \alpha_S \log S, \quad (10)$$

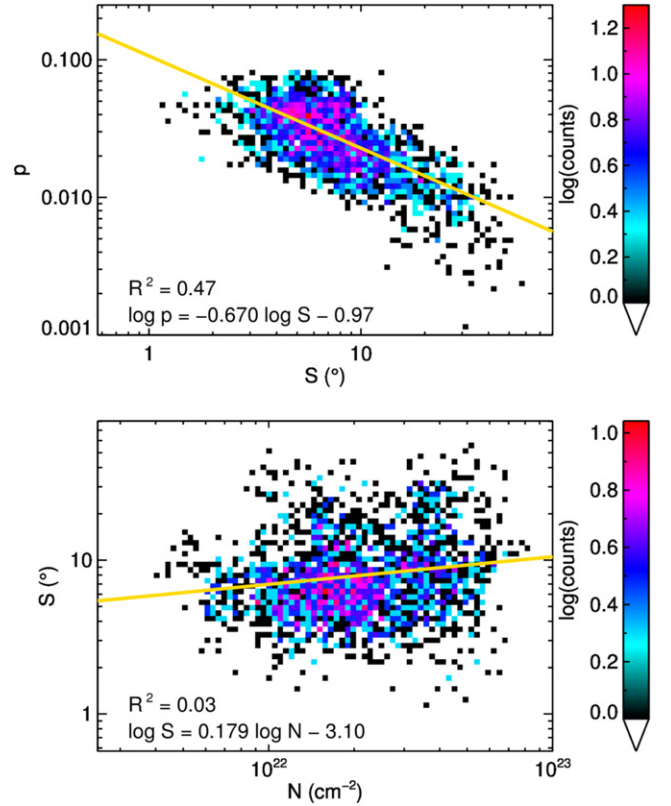


Figure 14. Two-dimensional histograms showing correlations between p , N , and S for ISRF-heated sightlines: p vs. S (top panel); and S vs. N (bottom panel). All data points used to make these plots passed the selection criteria described in 4.4. The color is proportional to the logarithm of the number of data points located within each bin. The solid lines show fits to the data (Section 7.1).

where K , α_N and α_S are the free parameters.

The exponents derived via a fit to Equation (10) are $\alpha_N = -0.45 \pm 0.01$ and $\alpha_S = -0.60 \pm 0.01$. Just as in Sections 6 and 7.1, errors in fit parameters are derived via bootstrapping (Table 2). We note that, as expected, α_N and α_S derived from the two-variable power-law fit to N and S are identical within the error bars to $\alpha_{p^{[S]}, N}$ (the power-law fit to $p^{[S]}$ as a function of N) and $\alpha_{p^{[N]}, S}$ (the power-law fit to $p^{[N]}$ as a function of S), which were derived in Section 7.1 (also see Table 1).

We can remove the dependence of p on N and S via

$$p_i^{[N, S]} = \frac{p_i \bar{p}}{p(N_i, S_i)}, \quad (11)$$

where $p_i^{[N, S]}$ is the decorrelated p for the i th data point, p_i is the measured polarization fraction for the i th data point, $p(N_i, S_i)$ is the value of the two-variable power-law fit for the i th data point, and $\bar{p} = 0.029$ is the median value of p . A comparison of the spatial distribution of p (middle panel) with $p^{[N, S]}$ (bottom panel) is shown in Figure 11. We discuss potential causes of residual structure in the $p^{[N, S]}$ map in Section 8.4.

Finally, we quantify the degree to which our two-variable power-law fit $p(N, S)$ can reproduce the observed dispersion in p . Figure 16 shows histograms of: our calculated $\log p$ (left panel); $\log p(N, S)$, the two-variable power-law fit values calculated for our N and S data points (center panel); and $\log p^{[N, S]}$, p with the derived dependence on N and S removed

Table 1
Power-law Exponents of p vs. N and S

Diffuse Emission Subtraction Method	α_N	α_S	$\alpha_{p^{[S]N}}$	$\alpha_{p^{[N]S}}$
Intermediate	-0.58 ± 0.02	-0.67 ± 0.02	-0.46 ± 0.01	-0.58 ± 0.01
Conservative	-0.53 ± 0.02	-0.67 ± 0.02	-0.39 ± 0.01	-0.56 ± 0.01
Aggressive	-0.66 ± 0.02	-0.66 ± 0.02	-0.57 ± 0.01	-0.59 ± 0.01

Note. The power-law exponents listed in this table are derived from linear fits of $\log p$ to $\log N$ and $\log S$ as described in Sections 6 and 7.1.

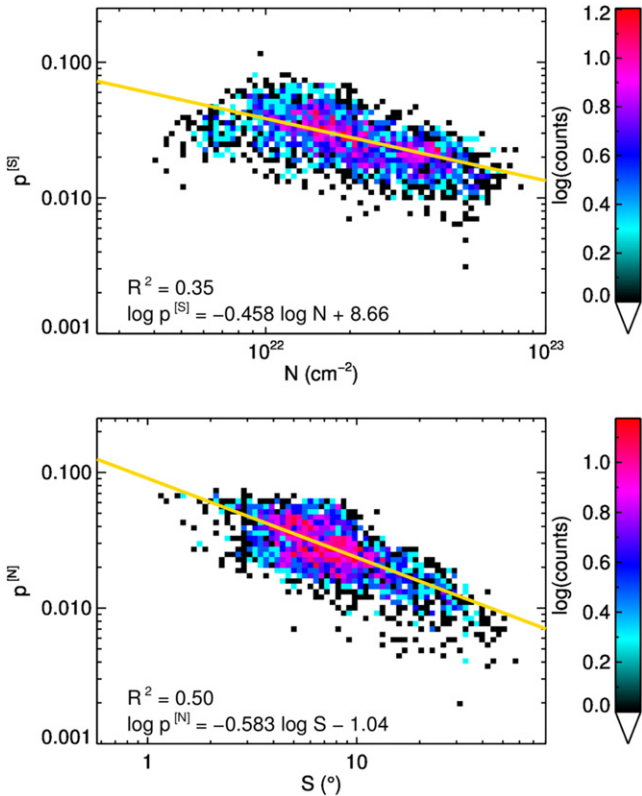


Figure 15. Two-dimensional histograms showing decorrelated p as a function of N and S for ISRF-heated sightlines: $p^{[S]}$, the polarization fraction (p) with the dependence on S removed vs. N (top panel); and $p^{[N]}$, p with the dependence on N removed vs. S (bottom panel). The color is proportional to the logarithm of the number of data points within the bin. The solid lines show the linear fits to the data (Section 7.1).

Table 2
Fit Parameters of $p(N, S)$ from Equation (10)

Diffuse Emission Subtraction Method	α_N	α_S	K
Intermediate	-0.45 ± 0.01	-0.60 ± 0.01	8.42 ± 0.3
Conservative	-0.41 ± 0.01	-0.59 ± 0.01	6.92 ± 0.3
Aggressive	-0.58 ± 0.01	-0.60 ± 0.01	10.98 ± 0.3

Note. The power-law exponents (α_N and α_S) and fitted constant (K) listed in this table are calculated from a two-variable power-law fit to N and S as described in Section 7.2.

using Equation (11) (right panel). For each of the three cases the median p is 0.029. Histograms of $\log p$ rather than p are shown, because the fits are made in log space. The variances of

$\log p$, $\log p(N, S)$, and $\log p^{[N,S]}$ are 0.068, 0.045, and 0.023, respectively. Our model $\log p(N, S)$ reproduces 66% of the variance in the $\log p$ map, which shows that our two-variable power-law fit model captures most of the physical effects that determine variations in fractional polarization in Vela C.

7.3. Uncertainties in the Power-law Fit Exponents

The uncertainties of the exponents for the two-variable power-law fits α_N and α_S were estimated using the bootstrapping methods described in Section 6. However, as discussed in Section 3.5, the limiting uncertainty is our inability to precisely separate the contribution of background/foreground dust from the polarized emission of Vela C. We repeated our analysis for maps of p and S made with the “conservative” and “aggressive” diffuse emission subtraction methods, to gauge the systematic uncertainty of our derived power-law exponents. Table 1 gives power-law exponents derived from the individual correlations (Section 7.1) for the three different diffuse dust emission subtraction methods. Table 2 lists the exponents α_N and α_S of the two-variable power-law fits again for all three diffuse emission subtraction methods. Systematic uncertainties relating to the choice of subtraction method are seen to be ~ 0.1 for α_N and ~ 0.01 for α_S .

8. DISCUSSION

8.1. Implications of the Dependence of p on N and T

In Section 6 we examined the dependence of the polarization fraction p on column density N and dust temperature T in Vela C. We divided our Vela C sightlines into two groups: those that show evidence of heating from the compact H II region RCW 36, and those sightlines where the temperature decreases as $e^{-0.28N}$. For the latter sightlines we suggested that the dust temperature is primarily set by exposure to the interstellar radiation field (ISRF), with high N sightlines having on average more shielding and therefore receiving less heating per unit mass from the ISRF.

For the ISRF-heated sightlines, we find that p decreases with increasing N and also that p increases as T increases. Depolarization for higher column density sightlines has been seen in many studies (see Section 7.1). Vaillancourt & Matthews (2012) used the ratio of $F(850 \mu\text{m})/F(350 \mu\text{m})$ as a proxy for dust temperature in two massive star forming clouds. They found that the polarization tended to decrease with increasing $F(850 \mu\text{m})/F(350 \mu\text{m})$, implying that warmer dust grain populations tend to have a higher p . This agrees with our result, but Vaillancourt & Matthews (2012) caution that variations in $F(850 \mu\text{m})/F(350 \mu\text{m})$ could be due to changes in dust spectral index, rather than just dust temperature. Our study is the first to fit p measurements within a molecular cloud as a function of both N and T . For the ISRF-heated sightlines,

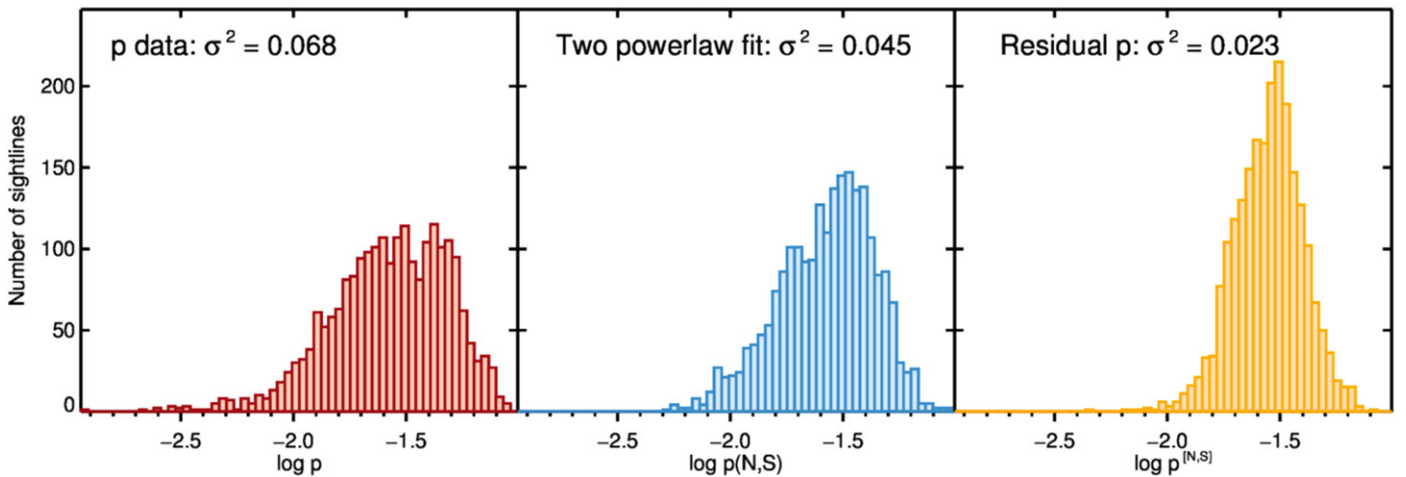


Figure 16. Histograms of the logarithms of p before decorrelation (left panel), $p(N, S)$ evaluated for N and S data using the model described in Equation (10) (center panel), and $p^{[N, S]}$, the residual structure in p after normalizing out $p(N, S)$ (right panel). The variance (σ^2) of the distribution is given at the top of each panel. The quantity $p^{[N, S]}$ was normalized so that the median p remained at 0.029 (see Equation (11)).

which are the majority of the sightlines, we find that the dependence of p on N is not separate from the dependence of p on T , since N and T are highly correlated.

There are two general classes of explanations for our observations of p versus N and T for the ISRF-headed sightlines. We may have greater magnetic field disorder along high N (and therefore lower T) dust columns, or we may have a decrease in the intrinsic polarization efficiency (see Section 1) for such sightlines. In the first explanation the increased field disorder could arise because of a higher field disorder at high particle densities n , or because high N sightlines pass through more cloud material and therefore may sample different field directions at different locations along the line of sight (Jones 1989). Regarding the second possible explanation for our observed p versus N and T trends, note that in the RATs model of grain alignment, “alignment torques” from an anisotropic radiation field are responsible for aligning the dust grain spin-axes with the local magnetic field (Lazarian & Hoang 2007). Grains near the surfaces of molecular clouds (low N , high T) thus might be expected to show a higher average polarization fraction (Cho & Lazarian 2005). Alternatively, dust grain properties could change at high densities, e.g., grains could become rounder due to accretion of icy mantles (Whittet et al. 2008).

For our RCW 36 heated sightlines there is a significant anticorrelation between p and N ($R^2 = 0.45$). However, for these heated sightlines there is no correlation between N and T and no strong correlation between p and T ($R^2 = 0.03$). This could indicate that the primary dependence of p is on N , rather than T and that the correlation of p with T only appears when there is a strong correlation of T with N . However, we caution that we have relatively few sightlines near RCW 36 (143 Nyquist-sampled sightlines compared to 2235 ISRF-heated sightlines) so the lack of correlation between p and T could be caused by the angle of the magnetic field changing with respect to the line of sight, which would cause more spread in p . Indeed Figure 5 shows that near RCW 36 there are significant changes in the inferred magnetic field orientation projected onto the plane of the sky.

8.2. Implications of the Two-variable Model $p(N, S)$

In Section 7.2 we fit a model that describes p as a function with a power-law dependence on two variables, hydrogen column density N , and S , the dispersion in the polarization-angle on scales corresponding to our beam FWHM (2.5, or 0.5 pc). The derived power-law exponents are $\alpha_N = -0.45 \pm 0.10$ for the dependence on N , and $\alpha_S = -0.60 \pm 0.01$ for the dependence on S (see Section 7.3). Our $p(N, S)$ fit is able to reproduce most of the structure seen in our $\log p$ maps.

The decrease in p with increasing S can be attributed to changes in the magnetic field direction within the volume probed by the BLASTPol beam. The mean magnetic field orientation, Φ , is an average over both the beam area (0.5 pc) and along the length of the cloud in the line of sight direction, and is weighted by the density and intrinsic polarization efficiency (Section 1). Large values of S indicate a substantial change in Φ on the scale of a beam, which implies a significant change in the orientation of polarization within the beam. This could be due to a sharp change in the magnetic field direction at some location within the cloud. Alternatively, it could indicate the overlap of two clouds, well separated along the line of sight, each with a different Φ . In either case we should see an overall decrease in the measured polarization fraction, since some of the polarization components cancel. Planck Collaboration Int. XX (2015) note a decrease of p with increasing S , both in their data and in corresponding MHD simulations (see Figure 19 of Planck Collaboration Int. XX 2015). However the *Planck* study sampled $5 \times 10^{20} \text{ cm}^{-2} < N < 10^{22} \text{ cm}^{-2}$ while our Vela C observations predominantly sample $10^{22} \text{ cm}^{-2} < N < 10^{23} \text{ cm}^{-2}$. Also direct comparison with their derived power-law exponents is difficult, since they fit S versus p , thus minimizing the scatter in S , while we fit p versus S , which minimizes scatter in p . Nevertheless they do find a significant anti-correlation of p and S in their data that is reproduced in their MHD simulations. In these simulations there is by contrast only a weak correlation of S with N (F. Levrier 2016, private communication), just as we found in our data (Figure 14, lower panel).

In Section 8.1, we discussed two classes of explanations for the observed p versus N trend. The first class involves

magnetic field disorder. An example is the work of Falceta-Gonçalves et al. (2008). These authors were able to reproduce a decrease in p with increasing N via synthetic polarization maps made from supersonic, sub-Alfvénic MHD molecular cloud simulations, assuming uniform intrinsic polarization efficiency. Their power-law exponents α_N ranged from 0 to -0.5 , with models where the mean magnetic field was in the plane of the sky ($\gamma = 0^\circ$) having the steepest slope and models where the mean field was parallel to the line of sight ($\gamma = 90^\circ$) having no dependence of p on N . In this theoretical study, the decrease in polarization for higher column density regions is due to an increase in the dispersion of the magnetic field direction for high density regions. An analytic model by Jones (1989), is similarly able to reproduce a falling p versus N for a medium having uniform intrinsic polarization efficiency.

Our analysis shows only a weak correlation (or perhaps no correlation) between S and N (see Section 7). Thus on 0.5 pc scales, we find no significant increase in the dispersion of Φ for sightlines of increasing column density. Such an increase might be expected if disorder in the magnetic field direction increased in high density regions (for example due to accretion-driven turbulence as in Hennebelle and André 2013), or if the magnetic field were affected by large-scale gas motions near self gravitating filaments. In the above-mentioned theoretical study by Falceta-Gonçalves et al. (2008), the authors showed that rarefied cloud regions show little variation in polarization direction whereas significant fluctuations in direction do occur within dense condensations. In this case, one might expect a positive correlation between S and N , which we do not see in our observations.

The second class of explanations for the observed decrease in p with increasing N involves changes in intrinsic polarization efficiency. This idea derives support from the observations of Whittet et al. (2008). These authors measured the near-IR polarization of background stars in four nearby molecular clouds. For studies of polarization of background starlight the quantity that is analogous to fractional polarization of dust emission is referred to as the “polarization efficiency,” defined as the fractional polarization of the starlight divided by the extinction optical depth at the same wavelength p_λ/τ_λ . Whittet et al. (2008) found that the polarization efficiency in their clouds was consistent with a power-law dependence, $p_\lambda/\tau_\lambda \propto A_V^{-0.52}$. Because the inferred magnetic field direction is mostly uniform across the region studied, they attributed all of the decrease in polarization efficiency with increasing N to changes in the intrinsic polarization efficiency. It is interesting to note that our power-law exponent ($\alpha_N = -0.45 \pm 0.10$) is similar to that found by Whittet et al. (2008). Other starlight polarization studies have found power-law exponent values ranging from -0.34 to -1.0 (Gerakines et al. 1995; Goodman et al. 1995; Arce et al. 1998; Chapman et al. 2011; Alves et al. 2014; Cashman & Clemens 2014; Jones et al. 2015). Ground-based studies of polarized thermal dust emission yield similar results. For example Matthews et al. (2002) examined p versus I_{850} for three clouds in Orion B south and found $p \propto (I_{850 \mu\text{m}})^\alpha$, with α ranging from -0.58 to -0.95 .

Which of the two general classes of explanations for the observed p versus N trend best explains our observations of Vela C? Naively, the absence of a correlation between S and N would suggest that magnetic field disorder does not

increase toward high N sightlines, which would imply that variation in intrinsic polarization efficiency is the more likely explanation. However, if the increased disorder in the field occurs on much smaller scales than 0.5 pc, the scale probed by S , then S is not sensitive to the random component of the field and so we would not expect a correlation between N and S . We emphasize that detailed statistical comparisons with simulations of magnetized clouds that include variations in intrinsic polarization efficiency are needed to fully understand the origin of the p versus N anticorrelation (e.g., Soler et al. 2013). Such comparisons are beyond the scope of the present paper.

8.3. Analytic Models of p versus N

In Section 8.2 we advanced various explanations for the anticorrelation between p and N in Vela C. Here we consider an extreme case where all of the dependence of p on N is due to reduced intrinsic polarization efficiency in shielded regions. Our goal is to quantify the ability of our measurements to trace magnetic fields deep inside the Vela C cloud under this pessimistic assumption. If most of the polarized emission comes from the outer diffuse layers of the cloud then our derived magnetic field orientations will not be sensitive to changes in the magnetic field direction within dense structures embedded deep in the cloud.

We model the efficiency of the dust along a given cloud sightline in emitting polarized radiation with ϵ , where epsilon is normalized such that $\epsilon = \xi \cos^2(\gamma)I/A_V$, where ξ is the intrinsic polarization intensity as defined in Section 1, A_V is the total dust extinction in the V band for that sightline, and γ is the angle of the magnetic field with respect to the plane of the sky. For these models $\epsilon = \epsilon(\chi)$, where χ is the parameterized depth into the cloud, which is equal to the integrated visual extinction to the nearest cloud surface as indicated in Figure 17. Note that these models make a number of assumptions: (a) that the cloud is isothermal; (b) that the dust emissivity does not change within the cloud; (c) that the magnetic field direction is uniform; and (d) that the geometry of the cloud is slab-like.

As the p versus N and p versus S trends appear to be independent (see Section 7) we compare predictions from our models with $p^{[S]}$, the polarization fraction decorrelated from S (Figure 15, upper panel). Figure 18 shows the predicted p from three models of $\epsilon(\chi)$ compared to our measurements of $p^{[S]}$ versus A_V , where here N has been converted to A_V assuming $N(H)/A_V = 2 \times 10^{21} \text{ cm}^{-2}$ (Bohlin et al. 1978 with $R_V = 3.1$). Because of the normalization of $p^{[S]}$ the overall level of polarization is somewhat arbitrary, but of the right order.

Here we describe the three plausible models of $\epsilon(\chi)$ shown in Figure 18:

Constant ϵ Model: if the intrinsic polarization efficiency were constant throughout the cloud we would expect no dependence of p on N . The best fit to this model is shown as a dashed-dotted line in Figure 18.

Skin Depth Model: alternatively, we can consider a model where the intrinsic polarization efficiency is constant up to an extinction depth χ_{crit} and zero thereafter; i.e., a diffuse layer near the cloud surface is responsible for all of the polarized emission and the dust at cloud depths above χ_{crit} does not contribute to the polarized emission. For a sightline of total

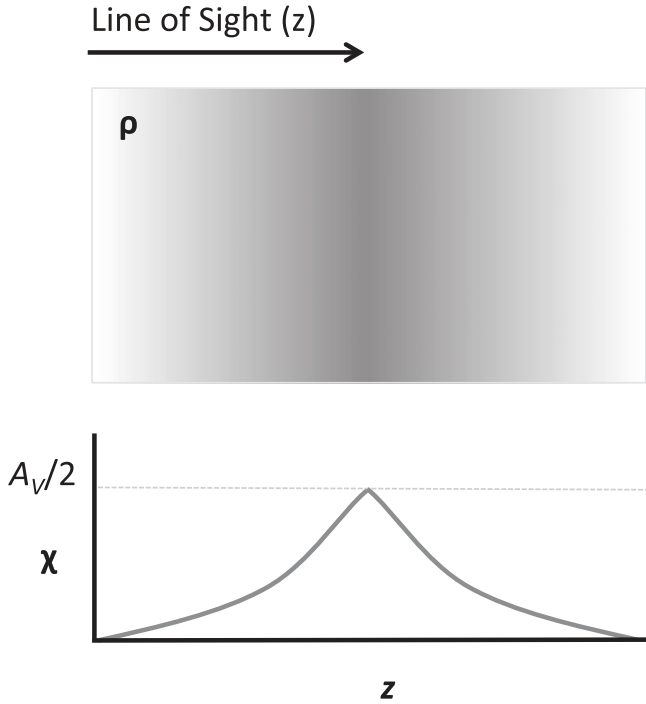


Figure 17. Cartoon showing the parameterized depth into the cloud χ for a slab model of a molecular cloud. The slab lies parallel to the plane of the sky. For a given position in the cloud along the line of sight (z) χ is equal to the integrated visual dust extinction to the nearest cloud surface. The maximum value of χ for a sightline of total visual extinction A_V is $A_V/2$.

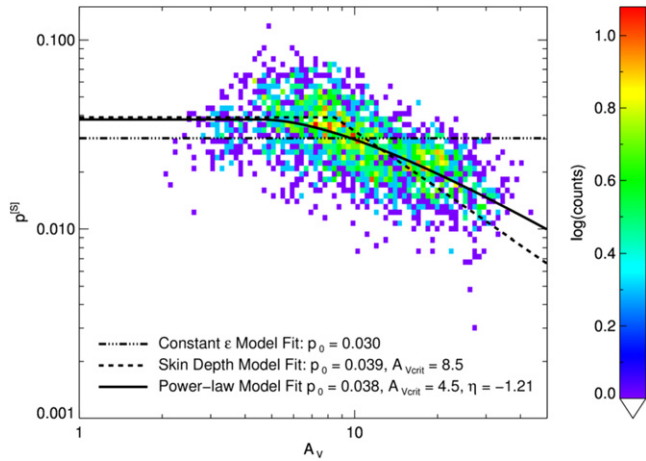


Figure 18. BLASTPol measurements of the polarization fraction with the dependence of S normalized out ($p^{[S]}$) vs. A_V . The solid line shows the results of a least-squares fit to the power-law decay intrinsic polarization efficiency (ϵ) model with derived parameters $p_0 = 0.038$, $A_{V,crit} = 4.5$ mag and $\eta = -1.21$. The dashed-dotted line shows a fit to the constant ϵ model with best-fit parameter $p_0 = 0.030$. The dashed line shows a fit to the “skin depth” ϵ model, where the best-fit parameters are $p_0 = 0.039$ $A_{V,crit} = 8.5$ mag.

extinction A_V the maximum value of χ is $A_V/2$. We express ϵ as

$$\epsilon(\chi) = \begin{cases} \epsilon_0, & \text{for } \chi \leq \chi_{crit}; \\ 0, & \text{for } \chi > \chi_{crit}, \end{cases} \quad (12)$$

where ϵ_0 is a constant, and from this we can calculate the total polarized intensity:

$$P = 2 \int_0^{A_V/2} \epsilon(\chi) d\chi = \begin{cases} A_V \epsilon_0, & \text{for } A_V \leq A_{V,crit}; \\ A_{V,crit} \epsilon_0, & \text{for } A_V > A_{V,crit}, \end{cases} \quad (13)$$

where we define $A_{V,crit} = 2\chi_{crit}$. The percentage polarization for a given sightline is then

$$p = \frac{P}{I} = \begin{cases} p_0, & \text{for } A_V \leq A_{V,crit}; \\ p_0 \frac{A_{V,crit}}{A_V}, & \text{for } A_V > A_{V,crit}. \end{cases} \quad (14)$$

In the “skin depth” model, p is constant for sightlines with $A_V \leq A_{V,crit}$ and decreases with a power-law slope of -1.0 for sightlines with $A_V > A_{V,crit}$. The dashed line in Figure 18 shows a fit to the skin depth model.

Power-law Model: finally we consider a model where the polarization efficiency is constant up to χ_{crit} and thereafter decreases as a power-law with coefficient η :

$$\epsilon(\chi) = \begin{cases} \epsilon_0, & \text{for } \chi \leq \chi_{crit}; \\ \epsilon_0 \left(\frac{\chi}{\chi_{crit}} \right)^\eta, & \text{for } \chi > \chi_{crit}. \end{cases} \quad (15)$$

This model simulates a constant ϵ for the diffuse outer cloud layers and a decreasing ϵ at greater cloud depths. The polarized intensity for a given sightline described by the power-law model is:

$$P = \begin{cases} \epsilon_0 A_{V,crit} a, & \text{for } a \leq 1; \\ \epsilon_0 A_{V,crit} \left(1 + \frac{1}{\zeta} [a^\zeta - 1] \right), & \text{for } a > 1, \end{cases} \quad (16)$$

where $\zeta = \eta + 1$ and $a \equiv A_V/A_{V,crit}$. The corresponding fractional polarization is then

$$p = \begin{cases} p_0, & \text{for } a \leq 1; \\ p_0 a^{-1} \left(1 + \frac{1}{\zeta} [a^\zeta - 1] \right), & \text{for } a > 1. \end{cases} \quad (17)$$

The power-law ϵ model best fit parameters are $p_0 = 0.038$, $A_{V,crit} = 4.5$ mag and $\eta = -1.21$ (Figure 18 solid line). Our power-law model fit would imply that at cloud depths of about two magnitudes or greater of visual extinction the intrinsic polarization efficiency decreases with depth into the cloud as $\sim \chi^{-1.21}$.

It can be seen that both the skin-depth and power-law model capture the negative slope of the $p^{[S]}$ versus N curve for high N . For the purposes of quantifying our ability to trace magnetic fields deep within the cloud, we will use the power-law model as it seems to more closely follow the data points in Figure 18. We also caution that these are all simple models, so the fits should be taken merely as indicative of the trends of ϵ with χ .

Using Equation (16) for a sightline of total dust extinction A_V we can calculate the fractional contribution to the polarized intensity from cloud material at depths of $< \chi'$

$$f(\chi') = \frac{P(\chi')}{P(\chi_{max})} \quad (18)$$

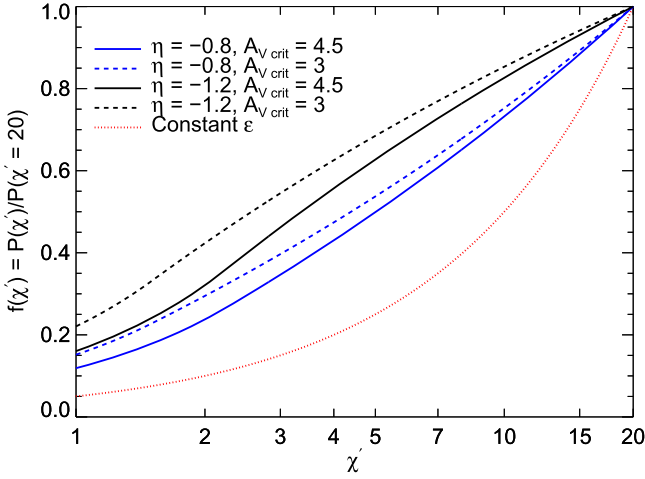


Figure 19. Models for the fraction of the total polarized intensity for a sightline of $A_V = 40$ mag ($\chi_{\max} = 20$ mag), contributed by all dust at cloud depths $< \chi'$ (see Equation (18)). The line color represents the power-law slope η assumed: -0.8 (blue); and -1.2 (black). Linestyle represents the $A_{V,\text{crit}}$ assumed: 3.0 mag (dashed); and 4.5 mag (solid). The red dotted line shows the expected $f(\chi')$ for dust of constant intrinsic polarization efficiency ϵ .

where by definition $\chi_{\max} = A_V/2$. Figure 19 shows $f(\chi')$ for a sightline of total dust extinction $A_V = 40$ mag (about the largest found in Vela C) over the range of $\chi' = 1$ to $\chi' = \chi_{\max} = 20$ mag. Dashed and solid lines represent different assumptions for $A_{V,\text{crit}}$, and line colors represent different power-law slopes η in Equation (16). The solid black line is derived using the best-fit parameters. For comparison we also show the expected behavior for the constant ϵ model (red dotted line). For our best fit parameters 27% of the polarized emission comes from the outer 2.2 mag of extinction, or the outer $2.2/20 = 11\%$ of the cloud. A further 47% of the total polarized emission comes from $2.2 \text{ mag} < \chi < 10 \text{ mag}$, which accounts for 39% of the dust column. The most deeply embedded regions of the cloud ($10 \text{ mag} < \chi < 20 \text{ mag}$) contribute 50% of the total dust column but only 27% of the total polarized emission. Figure 19 also shows that steeper power-law slopes and lower $A_{V,\text{crit}}$ values would imply that more of the total polarized intensity measured comes from the outer diffuse cloud layers.

To estimate the fraction of the cloud that, from the perspective of contributing to polarization, is “hidden” we first calculate the ϵ weighted mean cloud depth $\langle \chi \rangle$:

$$\langle \chi \rangle = \frac{\int_0^{A_V/2} \chi \epsilon d\chi}{\int_0^{A_V/2} \epsilon d\chi} = \frac{A_{V,\text{crit}}}{4} \frac{h(\chi)}{g(\chi)}, \quad (19)$$

where $g(\chi) = P/(\epsilon_0 A_{V,\text{crit}})$ (see Equation (16)) and $h(\chi)$ is given by

$$h(\chi) = \begin{cases} a, & \text{for } a \leq 1; \\ 1 + \frac{2}{\zeta+1}(a^\zeta - 1), & \text{for } a > 1. \end{cases} \quad (20)$$

If ϵ were constant throughout the sightline then $\langle \chi \rangle$ would equal half of the maximum value of χ giving $\langle \chi \rangle = A_V/4$. The fraction of the cloud that is hidden can then be roughly

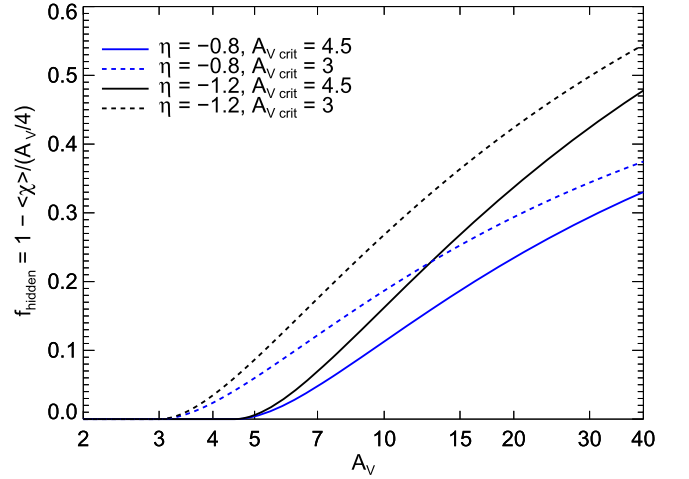


Figure 20. Fraction of the dust column that is hidden, i.e., not traced by polarized emission as a function of A_V as described by Equation (21). The line color indicates η and the linestyle indicates $A_{V,\text{crit}}$.

estimated as

$$f_{\text{hidden}} = 1.0 - \frac{\langle \chi \rangle}{A_V/4}, \quad (21)$$

which is shown in Figure 20. For $A_V = 10$ mag (assuming our best fit parameters) only 16% of the cloud is hidden. For a sightline of $A_V = 40$ mag about 48% of the cloud is hidden.

In summary, for “moderate” dust column sightlines ($A_V < 10$ mag) our polarization measurements sample most of the cloud ($f_{\text{hidden}} < 16\%$). So for sightlines with dust columns of $A_V \sim 10$ mag or less, the BLASTPol $500 \mu\text{m}$ measurement of the magnetic field orientation should be representative of the density-weighted average magnetic field orientation along the sightline. For higher dust column sightlines, the fraction of the cloud that is not well sampled by our polarization measurements increases ($f_{\text{hidden}} \sim 34\%$ for $A_V = 20$ mag) and for our highest column sightlines ($A_V \sim 40$ mag) about half of the dust contributes little to the polarization measured by BLASTPol. For these latter sightlines BLASTPol would not be sensitive to changes in magnetic field direction in the most deeply embedded cloud material. Recall that our model assumes that all of the decrease in p with N is due to lower intrinsic polarization efficiency of material deep within the cloud. If some of the decrease in p with N is due to increased field disorder along high N sightlines then the ϵ drop-off with χ would be shallower, which would decrease the fraction of the cloud that is hidden.

As noted earlier, our model has many implicit assumptions (slab-geometry, uniform dust temperature, power-law dependence of $\epsilon(\chi)$). In particular, the assumption of isothermality is clearly incorrect. Figure 10 shows that for the ISRF-heated sightlines included in this analysis the average temperature decreases with increasing column density (and thus increasing A_V). For the temperature extremes of 11 K and 15 K of the ISRF sightlines in Figure 10, we calculate that for the colder highest column density sightlines the dust on average emits half as much radiation per unit mass at $500 \mu\text{m}$ compared with dust on the warmer more diffuse cloud sightlines. It is quite likely that the more deeply embedded dust grains in Vela C are colder, which implies they will contribute less than warmer grains near the cloud surfaces to both the total intensity and the

measured polarized intensity. We therefore expect that the average magnetic field orientation inferred from polarization data will be weighted more toward the orientation in the warmer regions of the cloud. This will increase f_{hidden} : even assuming uniform intrinsic polarization efficiency if the outer half of the dust grains had $T = 15$ K and the inner half of the dust grains had $T = 11$ K then we find that $f_{\text{hidden}} = 20\%$.

To some degree this problem can be reduced by measuring polarization at millimeter wavelengths where the intensity of thermal dust emission is less sensitive to temperature. For detailed statistical comparisons of submillimeter polarization data with synthetic observations of molecular clouds derived from numerical simulations it will be important to not only model the effects of grain alignment in simulation postprocessing but also include a realistic cloud temperature structure. Due to the aforementioned uncertainties that are related to the assumptions in our model, our values of f_{hidden} should be taken only as crude estimates.

Despite these uncertainties, we note that, our results are consistent with the findings of Cho & Lazarian (2005), who showed that dust grains can be aligned efficiently by RATs at cloud depths χ of up to 10 mag in visual extinction. Bethell et al. (2007) found that the exact depth to which grains are aligned depends on grain size and on the degree of anisotropy of the local radiation field. Our model is also consistent with recent observations by Alves et al. (2014) who argue that their observations of submillimeter polarization of a starless core suggest loss of grain alignment at column densities higher than $A_V = 30$ mag. If ϵ changes appreciably with χ in the cloud then this might be revealed in the frequency dependence of p . Thus studying p at higher frequencies, as can be done using BLASTPol data, might provide further constraints.

8.4. Possible Causes of the Residual Structure in $p^{[N,S]}$

In Section 7.2 we showed that we can account for most of the variations in p that we observe in Vela C with a simple two-variable power-law fit $p(N, S)$. Here, we consider a number of factors besides N and S which could contribute to the variance in p . The dispersion in the logarithm of the decorrelated fractional polarization $\log(p^{[N,S]})$ is 0.15, which corresponds to a variance in $p^{[N,S]}$ of 1.0×10^{-4} .

If the variance in p were entirely due to the measurement uncertainty, then we would expect the variance in p to be described by:

$$\sigma_{p \text{ stat}}^2 = \sqrt{\frac{\sum_i^n \sigma_{p_i}^2}{n}} = 1.7 \times 10^{-6}, \quad (22)$$

where $\sigma_{p_i}^2$ is the variance for each individual p_i and n is the total number of data points. This value for $\sigma_{p \text{ stat}}^2$ is much smaller than the measured variance in $p^{[N,S]}$. Measurement uncertainties thus play a minor part in the observed variance of $p^{[N,S]}$.

A more likely possibility is that the variance in $p^{[N,S]}$ seen in Figure 16 and the bottom panel of Figure 11 is the result of changes in the direction of the magnetic field with respect to the line of sight. The observed polarization of a population of dust grains aligned with respect to a uniform magnetic field depends on γ , the angle between the magnetic field direction

and the plane of the sky:

$$p = p_{\text{max}} \cos^2 \gamma, \quad (23)$$

where p_{max} is the polarization that would be observed if the magnetic field were parallel to the plane of the sky ($\gamma = 0^\circ$). Our inferred magnetic field maps (Figure 5) clearly show several large scale changes in magnetic field direction Φ . Corresponding large scale changes in γ would add width to the $\log p$ distribution. In theory a detailed statistical comparison of S and $p^{[N,S]}$ on different angular scales could be used to gain insight into the three-dimensional structure of the magnetic field. However, such a treatment is beyond the scope of the present paper.

9. SUMMARY

In this work we present 500 μm maps of the Vela C GMC from the 2012 flight of BLASTPol. Our polarization maps were calculated from Stokes I , Q and U maps with background/foreground diffuse polarized emission subtracted as described in Section 3.5. These maps were used to calculate the inferred magnetic field orientation Φ projected onto the plane of the sky. Overall we see a change in the magnetic field orientation across the cloud, from perpendicular to the main cloud elongation direction in the south, to nearly parallel to the cloud elongation in the north. We also see regions of sharp changes in the magnetic field direction, as traced by S , the average angular dispersion on scales corresponding to our beam (2/5 or 0.5 pc scales).

As a first step in our analysis of the Vela C data we examine the dependence of polarization fraction p as a function of column density N , dust temperature T , and local angular dispersion S for sightlines in four of the five cloud regions defined in Hill et al. (2011). The goal of this work is to look for empirical trends that can be compared to numerical simulations of molecular clouds. These trends can be used to learn about the magnetic field properties and intrinsic polarization efficiency within the cloud. As part of our analysis we separate our sightlines into those that appear to be primarily heated by the interstellar radiation field (ISRF) and the minority of sightlines that show evidence of heating from the compact H II region RCW 36.

Our main findings are as follows:

1. For the ISRF-heated sightlines we find that p is anticorrelated with N and correlated with T , i.e., the polarization fraction decreases with increasing column density, and increases with increasing dust temperature. However, N and T are also highly anticorrelated with one another and normalizing out the power-law dependence of p with N removes the correlation with T . In the absence of bright internal sources it is expected that the density structure of the cloud largely determines the observed T ; therefore we choose N as our independent variable in the subsequent analysis. For the RCW 36 heated sightlines where there is no correlation between N and T , we see no correlation between p and T but there is still a strong anticorrelation between p and N . This suggests that for the RCW 36 -heated sightlines the important variable controlling p is N .
2. We derive a two-variable power-law empirical model $p \propto N^{\alpha_N} S^{\alpha_S}$ for the ISRF-heated sightlines, where $\alpha_N = -0.45 \pm 0.10$ and $\alpha_S = -0.60 \pm 0.01$. This model can reproduce $\sim 66\%$ of the variance in $\log p$. The

decrease in p with increasing S is probably the result of changes in the magnetic field direction within the volume of the cloud sampled by the beam. The decrease in p with N could be caused by increased disorder in the magnetic field for high column density sightlines or changes in the intrinsic polarization efficiency (e.g., the fraction of aligned grains, or grain axis ratio) for deeply embedded cloud material.

3. We do not find a strong correlation between N and S . This suggests that the disorder in the magnetic field does not increase significantly with density, which would in turn imply that the explanation for the decrease of p with increasing N is reduced intrinsic polarization efficiency for high N sightlines. However, this might not be the case. It might be that there is more disorder in the magnetic field toward higher column density sightlines, but this disorder occurs on much smaller scales than 0.5 pc, the scale probed by S , such that S is not sensitive to the disordered magnetic field component.
4. As a limiting case we consider the implications if the decrease in p with increasing N is due solely to reduced intrinsic polarization efficiency along high column density sightlines. In this case our BLASTPol measurements of the magnetic field orientation Φ would preferentially sample the material closer to the surface of the cloud and be less sensitive to changes in the field direction in the highly extinguished regions deep within the cloud. We introduce a crude model in which the intrinsic polarization efficiency is uniform in the outer cloud layers and then drops with a power-law dependence on the parameterized cloud depth χ . From a fit of our observational data to this crude model we conclude that for sightlines having $A_V < 10$ mag, Φ is a reasonable measure of the average magnetic field direction along the line of sight, but for sightlines of $A_V = 40$ mag, much of the cloud (roughly the inner half) is not well traced by Φ . This model might be a “worst-case” scenario because some of the decrease of p with A_V could arise from effects of magnetic field geometry not included in the model (e.g., more structure in the magnetic field along high column density sightlines).
5. The remaining scatter in $p^{[N,S]}$, the polarization fraction with our derived power-law dependence on S and N normalized out, is too large to be explained by our measurement uncertainties in p , but could be explained by variations in the angle of the magnetic field with respect to the plane of the sky.

In this paper we have examined polarization trends for only one cloud. Other clouds with different properties, in particular different average angle γ of the magnetic field with respect to the plane of the sky, might show different trends. To better constrain numerical simulations of star formation, our two-variable power-law fit should be repeated for a wide variety of clouds, which will presumably encompass a range of γ values. Our study provides constraints for numerical simulations of molecular clouds; for at least one assumed value of γ synthetic polarization observations of the simulations should be able to reproduce (a) our two-variable power-law fit exponents and (b) the lack of correlation between N and S (on 0.5 pc scales).

The authors like to thank the referee for a detailed and thoughtful review that has helped to strengthen the paper. The

BLASTPol collaboration acknowledges support from NASA (through grant numbers NAG5-12785, NAG5-13301, NNGO-6GI11G, NNX0-9AB98G, and the Illinois Space Grant Consortium), the Canadian Space Agency (CSA), the Leverhulme Trust through the Research Project Grant F/00 407/BN, the Natural Sciences and Engineering Research Council (NSERC) of Canada, the Canada Foundation for Innovation, the Ontario Innovation Trust, the Dunlap Institute for Astronomy and Astrophysics, and the US National Science Foundation Office of Polar Programs. LMF was supported in part by an NSERC Postdoctoral Fellowship. BD is supported through a NASA Earth and Space Science Fellowship. CBN also acknowledges support from the Canadian Institute for Advanced Research. FPS is supported by the CAPES grant 2397/13-7. Z-YL is supported in part by NSF AST1313083 and NASA NNX14AB38G. FP thanks the Spanish Ministry of Economy and Competitiveness (MINECO) under the Consolider-Ingenio project CSD2010-00064. The authors would also like to thank Diego Falceta-Gonçalves for making available line integral convolution code, which was used in making the drapery image shown in Figure 5. Finally, we thank the Columbia Scientific Balloon Facility (CSBF) staff for their outstanding work.

APPENDIX A DETAILED DESCRIPTION OF NULL TESTS

We restrict consideration to the 250 μm maps for the purpose of the null tests because the larger number of detectors in this band allows coverage of the map area to remain complete even when splitting the data set in two. Furthermore, if the asymmetric beam shape is a significant source of systematics, these will be manifested more strongly at 250 μm , as the beam in this band is the least symmetric of the three. We would expect any regions that pass the null tests at 250 μm will also pass in the longer-wavelength bands.

TODs were split into single raster scans, representing one complete raster of BLASTPol over the target map area at one half-wave plate position. Once the total data set was segmented using one of the four criteria described in Section 3.6, separate maps of Stokes I , Q , and U were made with TOAST (Section 3.4) for each of the two categories. The diffuse emission removal described in Section 3.5 was then performed for each map. For each null test criterion, we examined three metrics for evaluating systematic disagreement between the data segments:

1. Polarization fraction (p): independent maps of p were produced using the I , Q , and U maps from each half of the data (p_A and p_B , where “A” and “B” generically represent the left and right sets, the early and late sets, etc.) A p residual map, Δp was calculated where $\Delta p = (p_A - p_B)/2$, the absolute value of which is absolute separation of each of p_A and p_B from the mean p , $(p_A + p_B)/2$. The quantity Δp was taken to represent the uncertainty in p due to systematic sources of error, and we looked for regions in the full-data map where the calculated p is greater than $3\Delta p$ for each of the 4 null tests described in Section 3.6.
2. Polarization angle (ψ): Analogously, two independent maps of ψ were calculated for each of the null tests (again, ψ_A and ψ_B , generically). Because a polarization measurement with 3σ confidence in Q and U has an uncertainty in ψ of about 10° , we looked for regions in

the full-data map where the absolute difference between ψ_A and ψ_B was less than 20° . This standard is equivalent to requiring that the polarization-angle from each of the two data halves be consistent with the mean of ψ_A and ψ_B .

3. Polarized intensity ($P = \sqrt{Q^2 + U^2}$): To examine systematic errors in P , we reproduced the procedure described in Section 3.4 of Matthews et al. (2014). Briefly, residual maps of Q and U were calculated as the difference between that parameter and its average value in the null test data halves. The Q and U residuals were then used to form a $P_{\text{res}} = \sqrt{Q_{\text{res}}^2 + U_{\text{res}}^2}$. As in the p metric described above, P_{res} was taken as the systematic uncertainty in P , and we required the full-data measurement of P to be greater than $3P_{\text{res}}$.

APPENDIX B POLARIZATION CONVENTIONS

In this paper we discuss the polarized component of the dust emission (P) and the fractional polarization of dust emission (p), both of which can be derived from the linear polarization Stokes parameters:

$$P = \sqrt{Q^2 + U^2}, \quad (24)$$

and

$$p = \frac{P}{I}. \quad (25)$$

The associated angle of the polarization ψ is

$$\psi = \frac{1}{2} \arctan(U, Q), \quad (26)$$

where the two argument arctan function computes $\arctan(Q/U)$ while avoiding the ambiguity when $Q = 0$ MJy sr^{-1} . The polarization angle ψ is defined from -90° to 90° . Our conventions for Q and U are such that 0° corresponds to North in Galactic coordinates and ψ increases East of Galactic North (counterclockwise). This follows the IAU conventions (Hamaker & Bregman 1996), but differs from the `HEALPIX`³¹ convention adopted for Planck data, where ψ increases West of Galactic North (clockwise). The apparent angle of the magnetic field projected on to the plane of the sky Φ is

$$\Phi = \psi + \frac{\pi}{2}. \quad (27)$$

It is important to note that Φ is a tracer of the cloud magnetic field direction that is weighted by the efficiency of polarized dust emission averaged over the BLASTPol beam and along the line of sight.

The variances of P , p and ψ are defined in Planck Collaboration Int. XIX (2015) (Equations (25)–(27)).

REFERENCES

- Alves, F. O., Frau, P., Girart, J. M., et al. 2014, *A&A*, 569, L1
- Andersson, B.-G., Lazarian, A., & Vaillancourt, J. E. 2015, *ARA&A*, 53, 501
- Arce, H. G., Goodman, A. A., Bastien, P., Manset, N., & Sumner, M. 1998, *ApJL*, 499, L93
- Bethell, T. J., Chepurnov, A., Lazarian, A., & Kim, J. 2007, *ApJ*, 663, 1055
- Bohlin, R. C., Savage, B. D., & Drake, J. F. 1978, *ApJ*, 224, 132
- Cabral, B., & Leedom, L. C. 1993, in Proc. 20th Annual Conf. on Computer Graphics and Interactive Techniques, SIGGRAPH '93 (New York: ACM), 263
- Cantalupo, C. M., Borrill, J. D., Jaffe, A. H., Kisner, T. S., & Stompor, R. 2010, *ApJS*, 187, 212
- Cashman, L. R., & Clemens, D. P. 2014, *ApJ*, 793, 126
- Chapman, N. L., Goldsmith, P. F., Pineda, J. L., et al. 2011, *ApJ*, 741, 21
- Chauvenet, W. 1863, A Manual of Spherical and Practical Astronomy (Philadelphia, PA: Lippincott)
- Cho, J., & Lazarian, A. 2005, *ApJ*, 631, 361
- Crutcher, R. M. 2012, *ARA&A*, 50, 29
- Dobashi, K., Uehara, H., Kandori, R., et al. 2005, *PASJ*, 57, 1
- Dotson, J. L. 1996, *ApJ*, 470, 566
- Falceta-Gonçalves, D., Lazarian, A., & Kowal, G. 2008, *ApJ*, 679, 537
- Galitzki, N., Ade, P. A. R., Angilè, F. E., et al. 2014, Proc. SPIE, 9145, 0
- Gandilo, N. N., Ade, P. A. R., Angilè, F. E., et al. 2015, *ApJ*, submitted (arXiv:1512.06745)
- Gerakines, P. A., Whittet, D. C. B., & Lazarian, A. 1995, *ApJL*, 455, L171
- Goodman, A. A., Jones, T. J., Lada, E. A., & Myers, P. C. 1995, *ApJ*, 448, 748
- Górski, K. M., Hivon, E., Banday, A. J., et al. 2005, *ApJ*, 622, 759
- Greenberg, J. M. 1968, in Interstellar Grains, ed. B. M. Middlehurst, & L. H. Aller (Chicago, IL: Univ. Chicago Press)
- Griffin, M. J., Bock, J. J., & Gear, W. K. 2002, *ApOpt*, 41, 6543
- Griffin, M. J., Swinyard, B. M., & Vigroux, L. G. 2003, Proc. SPIE, 4850, 686
- Hall, J. S. 1949, *Sci*, 109, 166
- Hamaker, J. P., & Bregman, J. D. 1996, *A&AS*, 117, 161
- Heiles, C. 2000, *AJ*, 119, 923
- Hennebelle, P., & André, P. 2013, *A&A*, 560, A68
- Hildebrand, R. H. 1983, *QJRAS*, 24, 267
- Hildebrand, R. H. 1988, *QJRAS*, 29, 327
- Hill, T., Longmore, S. N., Pinte, C., et al. 2010, *MNRAS*, 402, 2682
- Hill, T., Motte, F., Didelon, P., et al. 2011, *A&A*, 533, A94
- Hill, T., Pinte, C., Minier, V., Burton, M. G., & Cunningham, M. R. 2009, *MNRAS*, 392, 768
- Hiltner, W. A. 1949, *Sci*, 109, 165
- Jones, T. J. 1989, *ApJ*, 346, 728
- Jones, T. J., Bagley, M., Krejny, M., Andersson, B.-G., & Bastien, P. 2015, *AJ*, 149, 31
- Kowal, G., Lazarian, A., & Beresnyak, A. 2007, *ApJ*, 658, 423
- Lazarian, A. 2007, *JQSRT*, 106, 225
- Lazarian, A., & Hoang, T. 2007, *MNRAS*, 378, 910
- Li, H., Griffin, G. S., Krejny, M., et al. 2006, *ApJ*, 648, 340
- Liseau, R., Lorenzetti, D., Nisini, B., Spinoglio, L., & Moneti, A. 1992, *A&A*, 265, 577
- Matthews, B. C., Fiege, J. D., & Moriarty-Schieven, G. 2002, *ApJ*, 569, 304
- Matthews, B. C., Wilson, C. D., & Fiege, J. D. 2001, *ApJ*, 562, 400
- Matthews, T. G., Ade, P. A. R., Angilè, F. E., et al. 2014, *ApJ*, 784, 116
- McKee, C. F., & Ostriker, E. C. 2007, *ARA&A*, 45, 565
- Moncelsi, L., Ade, P. A. R., Angilè, F. E., et al. 2014, *MNRAS*, 437, 2772
- Montier, L., Plaszczyński, S., Levrier, F., et al. 2015, *A&A*, 574, A135
- Mouschovias, T. C., & Ciolek, G. E. 1999, in NATO Advanced Science Institutes (ASI) Series C, Vol. 540, ed. C. J. Lada, & N. D. Kylafis (Dordrecht: Kluwer), 305
- Murphy, D. C., & May, J. 1991, *A&A*, 247, 202
- Myers, A. T., Klein, R. I., Krumholz, M. R., & McKee, C. F. 2014, *MNRAS*, 439, 3420
- Netterfield, C. B., Ade, P. A. R., Bock, J. J., et al. 2009, *ApJ*, 707, 1824
- Novak, G., Dotson, J. L., & Li, H. 2009, *ApJ*, 695, 1362
- Palmeirim, P., André, P., Kirk, J., et al. 2013, *A&A*, 550, A38
- Pascale, E., Ade, P. A. R., Bock, J. J., et al. 2008, *ApJ*, 681, 400
- Planck Collaboration Int. XIX 2015, *A&A*, 576, A104
- Planck Collaboration Int. XX 2015, *A&A*, 576, A105
- Planck Collaboration Int. XXXIII 2016, *A&A*, 586, A136
- Planck Collaboration Int. XXXV 2016, *A&A*, 586, A138
- Press, W. H., Teukolsky, S. A., Vetterling, W. T., & Flannery, B. P. 1992, Numerical Recipes in C: The Art of Scientific Computing (2nd ed.; Cambridge: Cambridge Univ. Press)
- Roussel, H. 2013, *PASP*, 125, 1126
- Roy, A., Ade, P. A. R., Bock, J. J., et al. 2011, *ApJ*, 730, 142
- Soler, J. D., Hennebelle, P., Martin, P. G., et al. 2013, *ApJ*, 774, 128
- Vaillancourt, J. E., & Matthews, B. C. 2012, *ApJS*, 201, 13
- Wardle, J. F. C., & Kronberg, P. P. 1974, *ApJ*, 194, 249
- Whittet, D. C. B., Hough, J. H., Lazarian, A., & Hoang, T. 2008, *ApJ*, 674, 304
- Yamaguchi, N., Mizuno, N., Saito, H., et al. 1999, *PASJ*, 51, 775

³¹ <http://healpix.jpl.nasa.gov>; Górski et al. (2005).